

1 **Measurements of Forbush decrease events at the center**
2 **of the South Atlantic Magnetic Anomaly with Muon**
3 **detectors**

4 **Jorge Molina^{1,2}, Euan Richard¹, Giovanni Secchia¹, Diego Stalder¹, Matias**
5 **Bertoli¹, Caleb Trepowski¹, Oscar Baez¹, Carlos Benitez Montiel³, Lucas**
6 **Cho¹, Esteban Cristaldo⁴, Pio Barrios¹, Jesus Nunez⁵ and Alan Cuevas¹**

7 ¹Facultad de Ingeniería, Universidad Nacional de Asunción, Campus de la UNA, San Lorenzo, Paraguay

8 ²Autoridad Reguladora Radiológica y Nuclear-ARRN, Campus de la UNA, San Lorenzo, Paraguay

9 ³Instituto de Física Corpuscular (IFIC), CSIC Universitat de València, Calle Catedrático José Beltrán, 2,

10 46980 Paterna, Valencia

11 ⁴Istituto Nazionale di Fisica Nucleare, Sezione di Milano Bicocca, I-20126, Milano

12 ⁵National Institute for Space Research - INPE, São José dos Campos, SP

13 **Key Points:**

- 14 • Commissioning of a compact muon detector in Paraguay.
15 • Demonstration that the detector works correctly through the measurements of the
16 muon angle distribution and with muon flux measurement.
17 • Correlation with Forbush decrease using Truncated Time Shift statistical test.

18 **Abstract**

19 We present the construction and validation of a low-cost muon detector in Paraguay,
 20 located at the center of the South Atlantic Magnetic Anomaly (SAMA), where the ge-
 21 omagnetic cutoff rigidity R is 9.63 GV. The detector consists of plastic scintillator plates
 22 coupled with silicon photomultipliers (SiPMs) for light detection. To verify its perfor-
 23 mance, we measured the average muon flux rate and investigated its correlation with ge-
 24 omagnetic activity, particularly the disturbance storm time (Dst) index, during the May
 25 and October 2024 Forbush Decrease (FD) events. Using the Truncated Time-Shift (TTS)
 26 test – a recent statistical method for comparing time-series – we found a strong corre-
 27 lation, indicating our detector reliably measures the muon flux over time. Our measure-
 28 ments also allowed us to resolve the detailed morphology of the Forbush decreases, by
 29 comparison with local magnetic field fluctuations. These initial results represent a step
 30 forward in ground-level radiation monitoring within the SAMA, and highlight the po-
 31 tential of economical muon detectors as components of early-stage diagnostic systems
 32 for space weather forecasting.

33 **Plain Language Summary**

34 The Earth's magnetic field protects humans and technology from radiation com-
 35 ing from outer space. However, it can be affected by "space weather" events such as so-
 36 lar flares. The field also has a weak spot above central South America, and satellites have
 37 been damaged while moving through this region. We constructed a particle detector at
 38 ground level in Paraguay, at the center of this weak spot. It can monitor several types
 39 of particles, including muons and gamma rays.

40 We measured the arrival rate of muons and compared it to both the magnetic field
 41 itself and neutron radiation measured by other detectors on Earth's surface. When other
 42 detectors identified space weather events, we also observed a drop in the muon rate at
 43 our detector. This showed that our new detector can contribute to the detection and mon-
 44 itoring of space weather events and effects within the magnetic field's weak spot.

45 **1 Introduction**

46 Cosmic rays interacting with Earth's atmosphere produce extensive air showers made
 47 up of secondary particles, including muons, which can reach the surface. Such particles
 48 are monitored at ground level, and can provide insights into geomagnetic and space weather
 49 phenomena.

50 Transient disturbances in the interplanetary magnetic field (IMF), which are of-
 51 ten linked to solar events such as coronal mass ejections (CMEs), can temporarily shield
 52 Earth from cosmic radiation. This phenomenon results in particularly strong and sud-
 53 den reductions in particle fluxes observed on Earth, referred to as Forbush decreases (FDs)
 54 (Kilifarska et al., 2020). Initially observed more than 85 years ago (Cane, 2000), FDs con-
 55 tinue to serve as an important indicator of geomagnetic storms, and may have applica-
 56 tions in space weather forecasting (Papailiou et al., 2024).

57 Forbush decreases are also observed in geomagnetic measurements, such as the Dis-
 58 turbance Storm Time (Dst) index (Nose et al., 2015). This is a combined measurement
 59 of Earth's magnetic ring current at various sites around the equator, and is a commonly-
 60 used if somewhat simplified (Borovsky & Shprits, 2017) indicator representing the level
 61 of overall geomagnetic activity.

62 Ground level particle flux is observed by a diverse global array of ground level de-
 63 tectors, employing different technologies, and covering a range of geomagnetic cutoff rigidi-
 64 ties. Some of these are linked to global networks such as the Global Muon Detector Net-
 65 work (GMDN) (Rockenbach et al., 2014) and the Neutron Monitor Database (NMDB)
 66 (Klein et al., 2010).

67 1.1 The South Atlantic Magnetic Anomaly

68 Such detectors may be particularly valuable in the SAMA, a region of low mag-
 69 netic rigidity (Pavón-Carrasco & De Santis, 2016), where MeV protons and electrons trapped
 70 in the Van Allen rings can precipitate towards the upper layers of the atmosphere. These
 71 particles are known to directly impact and damage satellites (Finlay et al., 2020) and
 72 upon reaching the ionosphere they can cause further particle showers, damaging the ozone
 73 layer (Pinto et al., 1990) and potentially increasing radiation at ground level.

74 Figure 1 shows that Paraguay is at the center of the SAMA, where the magnetic field
 75 currently has only half the strength as would be expected from the magnetic dipole
 76 model. Measuring the muon flux and geomagnetic conditions here can help us further
 77 understand the behaviour of particle showers and hazardous effects in the region.

78 The figure is based on estimates from the CHAOS-7 model (Finlay et al., 2020),
 79 using satellite data from ESA's Swarm mission (Friis-Christensen et al., 2006), and is
 80 reproduced from Finlay et al. (2020) under a Creative Commons CC BY 4.0 license (avail-
 81 able at <https://creativecommons.org/licenses/by/4.0/>).

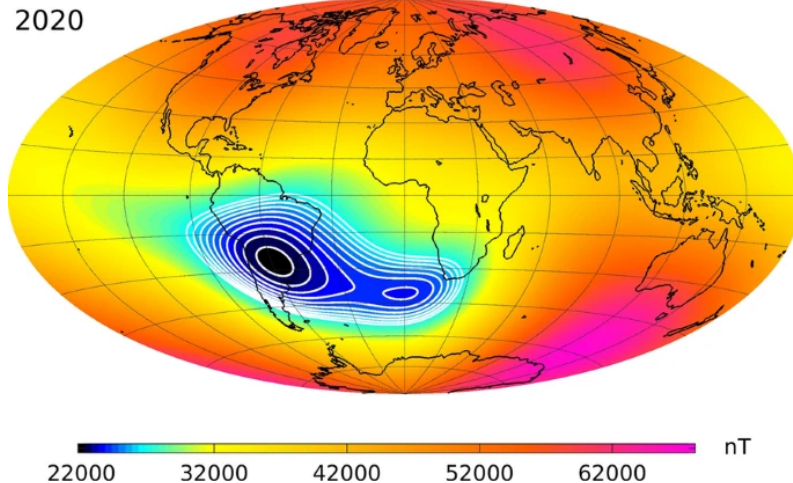


Figure 1: Magnetic field intensity at Earth's surface in 2020.

82 Forbush events have previously been measured inside the SAMA – for example the
 83 Muon detector at São Martinho da Serra in southern Brazil (part of the GMDN) detected
 84 an FD event during the November 2004 geomagnetic storm (Frigo et al., 2007). Since
 85 then, the the Tupi telescope (Augusto et al., 2012) in Niteroi, and the Muonca detec-
 86 tor (Fauth, 2016) in Campinas, have also recorded FD events. Further muon flux mea-
 87 surements, studying various aspects such as the day/night asymmetry, the time of flight,
 88 and the influence of atmospheric conditions on the arriving flux, have also been performed
 89 (Schuch, 2013), (Augusto et al., 2010).

90 1.2 The FIUNA Muon Detector

91 In this work we demonstrate that a relatively small and economical detector can
 92 measure the muon flux with sufficient sensitivity to detect space weather events. Our
 93 detector is stationed in the campus of the Facultad de Ingeniería de la Universidad Na-
 94 cional de Asunción (FIUNA), with coordinates -25.330°N -57.519°W at an altitude of 132 m,
 95 close to the center of the SAMA.

96 1.3 Contents

97 In Sec. 2 we present further details of the detector and electronics; in Sec. 3 dis-
 98 cuss data preparation and processing; in Sec. 4 discuss a methodolg to analyse the muon
 99 flux, and compare it with geomagnetic activity over time using a novel statistical tech-
 100 nique; in Sec. 5 we present the analysis results, and in Sec. 6 we discuss the implications
 101 and potential use of such measurements, and suggest future works.

102 2 Detection System

103 This section presents an overview of the design and operation of the muon detec-
 104 tor system at FIUNA. The architecture consists of three main components: (1) the phys-
 105 ical construction of the scintillator-based detection layers, (2) the signal conditioning elec-
 106 tronics that prepare raw SiPM outputs for digital interpretation, and (3) the data ac-
 107 quisition system that records, processes, and stores time-resolved particle detection events.
 108 The combination of these subsystems allows identification of coincident muon events with
 109 sub-microsecond resolution.

110 2.1 Physical Construction

111 The muon detector, as described in more detail in (Bertoli et al., 2023), consists
 112 of three $50 \times 50 \text{ cm}$ plastic scintillators, stacked above each other at 5 cm intervals, with
 113 each plate embedded to four SiPMs by a bezel on each corner. To suppress low-energy
 114 electrons, a 1 cm-thick iron absorber is inserted between the second and third scintil-
 115 lator layers. Figure 2 shows the three scintillator plates enclosed in black plastic during
 116 operation to protect it from external light sources.



Figure 2: Photograph of the muon detector, showing the three vertically stacked scintillator plates, each with SiPMs embedded at their four corners. A 1 cm thick iron plate is positioned between the second and third scintillator layers.

117 The scintillator material is Eljen EJ-200 (Eljen Technology, 2024), the SiPMs are
 118 Hamamatsu S13360-6050VE (“MPPC (Multi-Pixel Photon Counter) S13360-2050VE/-

119 3050VE/-6050VE”, 2024), which have a breakdown voltage of 53 ± 5 V and a temperature
 120 coefficient of 54 mV/ $^{\circ}$ C, and the FPGA board is a Digilent Basys 3 (Digilent, 2024).

121 Each SiPM is independently connected to the conditioning board, then to an FPGA
 122 board connected to a computer for data acquisition (DAQ). Figure 3 presents a block
 123 diagram of the muon detection system, detailing the sequential transformation of the sig-
 124 nals as it progresses through each stage. The silicon photomultipliers (SiPMs) act as trans-
 125 ducers, converting incident photons into pulse-like electrical signals. Subsequent stages
 126 are responsible for amplifying and shaping these pulses, and ultimately registering them
 127 as discrete counts stored in the local database.

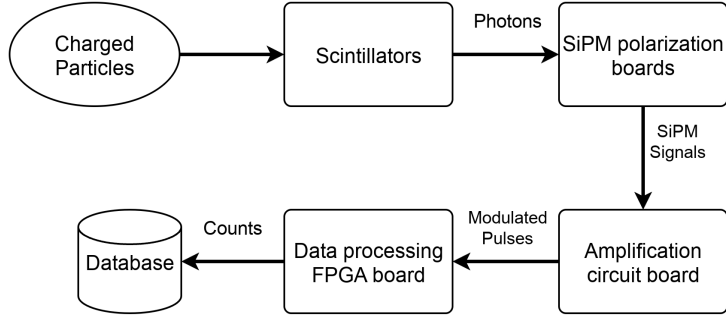


Figure 3: Block diagram illustrating the signal flow through the various stages of the muon detector.

128 2.2 Signal Processing

129 The signal conditioning process is divided into seven distinct stages, as illustrated
 130 in Figure 4. Detailed descriptions and schematics for each stage are shown in Appendix
 131 A.

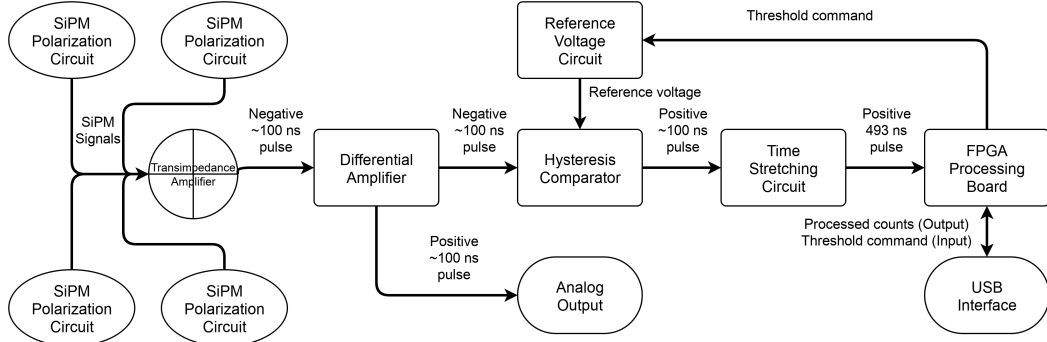


Figure 4: Block diagram illustrating the amplifying board stages for a single channel.

132 The signal conditioning board supports four independent channels, each capable
 133 of receiving four SiPM inputs. The outputs from these channels carry modulated pulses
 134 and are routed to separate inputs on the Basys3 FPGA board. This design provides flex-
 135 ibility for different configurations. In the current setup, three channels are used, each cor-
 136 responding to a scintillator plate, while one channel remains unused.

137 **2.3 Data Acquisition**

138 The FPGA board receives the amplified and stretched signal pulses, and a rising
 139 edge detector initiates the internal register-loading process. This functionality was de-
 140 veloped using VIVADO (AMD, 2024c), with a MicroBlaze microcontroller (AMD, 2024a)
 141 programmed in C through the VITIS environment (AMD, 2024b). The system records
 142 each scintillator channel trigger for single-channel events, and then within a 100 ns time
 143 window, using a match detector block, stores coincidences involving two or three chan-
 144 nels, or anticoincidences, as illustrated in Figure 5.

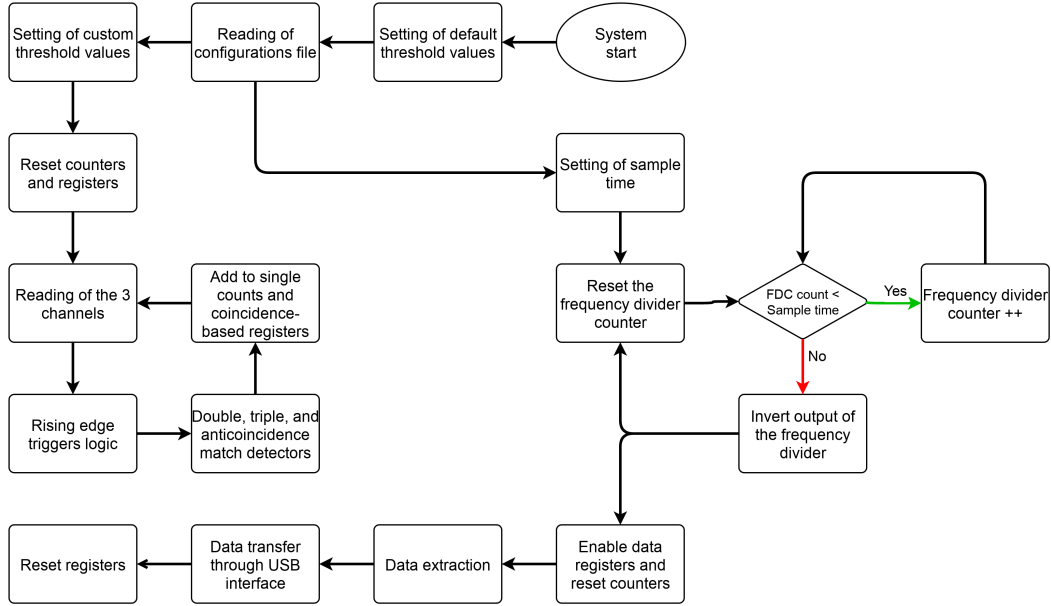


Figure 5: Algorithm implemented in the FPGA board using the verilog descrip-
 tion language.

145 Each possible trigger combination is stored in a dedicated 32-bit register. These
 146 registers are sequentially read through a multiplexer and sent to the FPGA board's UART
 147 module at the end of each sampling cycle. This process is governed by a timing loop set
 148 to a one-second interval. The FPGA board is connected via USB to a local computer,
 149 which polls the data every second, triggering register readout, reset, and storage of the
 150 collected values in a buffer file. A separate program running on the computer transfers
 151 the buffered data to an SQL database, clearing the buffer every minute. Logic blocks such
 152 as rising edge detectors, frequency dividers, match detectors, and multiplexers were adapted
 153 from standard VIVADO components to meet the specific frequency and channel require-
 154 ments of this system.

155 **3 Data Preparation**

156 This section outlines the preparation, correction, and validation processes for the
 157 muon flux data utilized in this study. We start by detailing the data acquisition peri-
 158 ods and preprocessing steps, including binning and deadtime filtering.

159 We then describe the calibration and correction process applied to our Muon count
 160 rate. It is known that the efficiency of SiPM detectors has an operating temperature de-
 161 pendence (Dinu, 2016). Additionally, before comparison with space weather phenomena,
 162 it is standard (Kovylyaeva et al., 2013; Riádigos et al., 2020) for ground-level detectors

163 to correct for atmospheric influences on particle shower propagation, in order to recon-
 164 struct the primary impinging flux. Therefore, we describe the application of a multivariate
 165 count-rate correction process for lab temperature, atmospheric temperature, and at-
 166mospheric pressure, which allows us to remove the environmental noise from our data,
 167 and produce a corrected muon count rate which we may compare directly with geophys-
 168ical and space weather phenomena.

169 3.1 Dataset Periods

170 As of 2024-05-27, the detector reached a stable configuration and tuning, and has
 171 since been in mostly continuous operation. Our initial data analysis was performed on
 172 the period from 2024-05-07 to 2024-06-24. A second analysis was later performed, us-
 173 ing an identical analysis technique, on data from 2024-09-16 to 2024-10-31. Therefore,
 174 we report results for both periods in this paper.

175 3.2 Deadtime Removal and Binning

176 The muon count rates were originally recorded each second. During the selected
 177 time periods, any intervals where the detector was not functioning reliably (known as
 178 “deadtime”) were excluded from the analysis. All sources of detector deadtime were ex-
 179 plicitly identified, including DAQ computer failures, faulty cables, test runs, and system
 180 restarts.

181 For analysis purposes, the data was then binned into 1-hour intervals. Any hourly
 182 bin with more than 60 s of deadtime was discarded. For bins with between 1 and 60 s
 183 of deadtime, the muon count was rescaled according to the number of operational sec-
 184 onds within that hour.

185 3.3 Environmental Corrections

186 3.3.1 Atmospheric Pressure Correction

187 Atmospheric pressure P and observed cosmic ray intensity at ground level I ex-
 188 hibit an inverse relationship. Typically, a linear correlation between pressure and the *frac-*
 189 *tional* change in intensity is considered sufficient to correct for this effect (Dorman, 1974):

$$\frac{dI}{I} \propto dP. \quad (1)$$

190 Thus, the pressure-corrected muon intensity I_{PC} can be approximated as a func-
 191 tion of the observed intensity I_{obs} as:

$$I_{\text{PC}}(t) = I_{\text{obs}}(t) \cdot e^{-\beta [P(t) - P_0]}$$

192 where $P(t)$ is the local atmospheric pressure at time t , P_0 is the mean pressure dur-
 193 ing the analysis period, and β is a fitted correlation coefficient which can be expressed
 194 in units of %/hPa.

195 3.3.2 Atmospheric Temperature Correction

196 The atmospheric temperature effect can also be corrected for in an approximately
 197 linear fashion, however we further apply the improved “MSS” method (Mendonça et al.,
 198 2016), where the atmospheric temperature T is divided into altitude bands and weighted

as a function of altitude (and therefore mass). The “mass-weighted temperature” T_{MSS} is then given by the equation

$$T_{\text{MSS}} = \sum_{i=0}^n T_i \cdot w_i \quad (2)$$

where i is the index representing each altitude band (from ground level 0 to highest n), T_i is the temperature observed at altitude of band i , and w_i is the weight function:

$$w_i = \frac{x_i - x_{i+1}}{x_0} \quad (3)$$

where x_i is the atmospheric depth at the altitude of band i . Finally, a simple linear correction can be fitted and applied to give the temperature-corrected muon intensity I_{TC} :

$$\Delta I_{\text{TC}}(t) = \alpha \cdot \Delta T_{\text{MSS}}(t) \quad (4)$$

where α is the temperature coefficient in $(\% / K)$. We obtain our temperature data T_i from the National Oceanic and Atmospheric Administration (NOAA) (National Oceanic and Atmospheric Administration (NOAA), n.d.; National Centers for Environmental Prediction (NCEP), n.d.).

3.3.3 SiPM Temperature Correction

Thirdly, despite a temperature-controlled environment within the laboratory, remaining temperature fluctuations exist within a few degrees Centigrade, as monitored by an internal sensor. While the performance of SiPMs is known to exhibit a strong dependence on operating temperature, within this temperature range we expect only a $1 \sim 3\%$ variation in count rate (Dinu, 2016), which can also be modelled by an approximately linear relationship.

3.3.4 Final Combined Corrections

Our muon count rate therefore depends simultaneously on internal laboratory temperature, atmospheric temperature, and atmospheric pressure. Furthermore, these variables are expected to be strongly correlated with each other, and all of these correlations can be expressed in a linear equation. Therefore, we apply a simultaneous multivariate linear fit on the three variables for each analysis period, in order to reconstruct a final corrected muon count rate.

In Figure 6 we show the uncorrected muon count rate data, alongside atmospheric temperature and pressure and lab temperature, for both analysis periods separately.

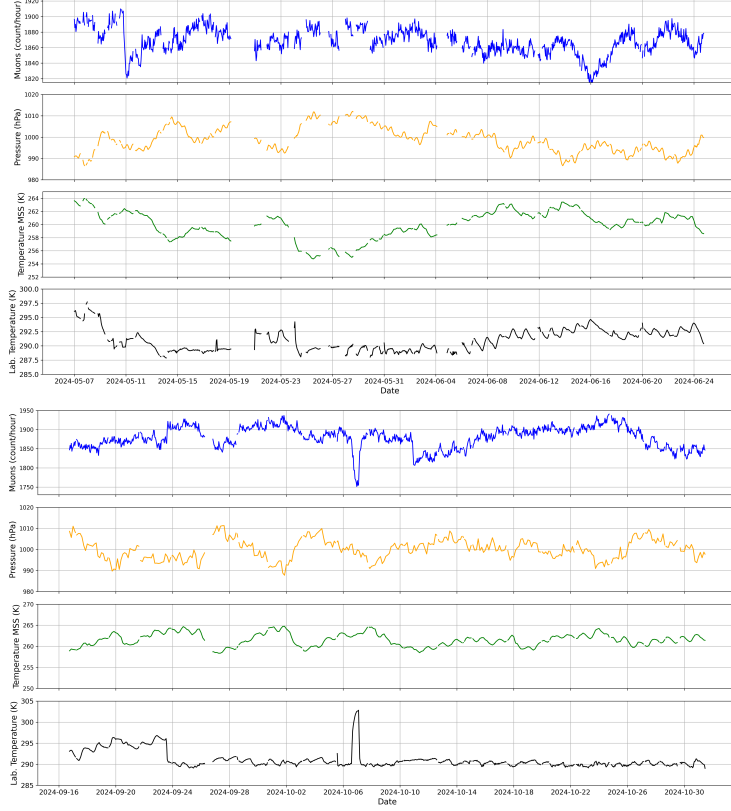


Figure 6: Uncorrected muon counts per hour, atmospheric pressure P , mass-weighted atmospheric temperature T_{MSS} , and laboratory temperature, for the analysis periods of May-June (top) and September-October (bottom).

The fitted multivariate linear correction coefficients are given in Table 1. On average the internal temperature provides the strongest correction, followed by atmospheric pressure; the atmospheric temperature provides the smallest correction, and in the second analysis period the correlation is statistically consistent with having no effect. The values are physically sensible, and when visualized describe the data well, therefore we consider this to be an accurate correction.

	Coefficient (May-Jun)	Coefficient (Sep-Oct)
Laboratory Temperature	$-0.202 \pm 0.02 \text{ \%}/\text{K}$	$-0.311 \pm 0.019 \text{ \%}/\text{K}$
Atmospheric Temperature	$-0.087 \pm 0.024 \text{ \%}/\text{K}$	$0.038 \pm 0.042 \text{ \%}/\text{K}$
Atmospheric Pressure	$-0.078 \pm 0.009 \text{ \%}/\text{hPa}$	$-0.119 \pm 0.013 \text{ \%}/\text{hPa}$

Table 1: Fitted multivariate linear correction coefficients per analysis period.

Finally, in Figure 7 we show the comparison between the uncorrected and corrected muon count rates. In most cases, the differences are relatively small. However, it should be noted that a particularly large trough is seen on 2024-10-07; unfortunately it is difficult to disentangle the physical implications of this, as the storm on this date caused an electrical blackout and a failure of the air conditioning units; this likely pushed the SiPM detectors outside of the temperature range where a linear correction was sufficient compensation.

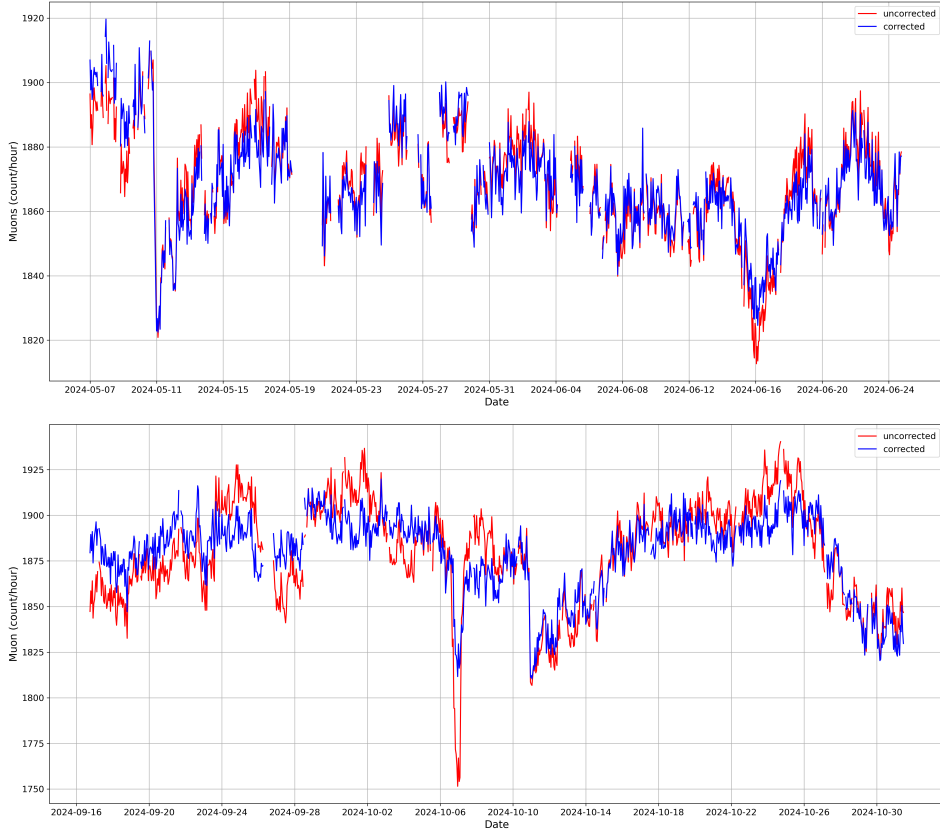


Figure 7: Uncorrected (red) and corrected (blue) muon hourly counts, for the analysis periods of May-June (top) and September-October (bottom).

240 4 Analysis Methodology

241 We perform two main analyses on our muon count data. First, we perform a mea-
 242 surement of the absolute muon flux at our detector location, by modelling the detector
 243 geometry and response, and atmospheric flux profile; this analysis combines both dataset
 244 periods. Second, we examine changes in muon count rate over time, especially during
 245 Forbush decrease events, and evaluate its relationship with the Dst index and local mag-
 246 netic field components. This section describes in detail the motivation behind each anal-
 247 ysis, and the methods used.

248 4.1 Muon Flux Measurement

249 Previous experiments around the globe (Borja et al., 2022) have shown that the
 250 muon flux arriving on the Earth’s surface roughly follows the distribution

$$I(\theta) = I_0 \cos^2 \theta \quad (5)$$

251 where θ is the zenith angle from 0 (vertically above the detector) to $\pi/2$ (the hori-
 252 zon), and I_0 represents the vertical flux intensity in units of $\text{m}^{-2} \text{s}^{-1} \text{sr}^{-1}$. The quantity
 253 I_0 is commonly measured and compared between experiments; a standard value is of-
 254 ten taken to be $82 \text{ m}^{-2} \text{s}^{-1} \text{sr}^{-1}$ (Greisen, 1942), but measurements have been reported
 255 in the range from 62 to 128, depending on location and altitude (Borja et al., 2022).

256 **4.1.1 Detector Geometry**

257 The general expression for the number of particles entering a detector per second
 258 requires integrating the flux over solid angle Ω and the surface area of the detector S as

$$\int_{\Omega} \int_S I(\omega) (\mathbf{r} \cdot \mathbf{n}) d\omega dS \quad (6)$$

259 where \mathbf{r} is the unit vector to the solid angle $d\omega$, \mathbf{n} is the normal vector to the sur-
 260 face dS , and it is assumed that $|\mathbf{r}| = 1$. This becomes easier to handle by switching to
 261 spherical coordinates (zenith θ , azimuth ϕ) for the incoming flux, and cartesian coordi-
 262 nates (x, y) for our detector's topmost surface, which is a simple 0.5 m wide square. The
 263 flux per second passing through all three scintillator plates on our detector may then be
 264 expressed as

$$I_D = \int_{x=0}^{0.5} \int_{y=0}^{0.5} \int_{\theta=0}^{\pi/2} \int_{\phi=0}^{2\pi} I(\theta) \cos(\theta) \sin(\theta) A_B(\theta, \phi, x, y) d\phi d\theta dy dx \quad (7)$$

265 where $\cos(\theta)$ comes from the surface dot product, $\sin(\theta)$ from the Jacobian of the
 266 coordinate transformation, and A_B is the binary acceptance function of 0 or 1 — which
 267 accounts for the fact that an incoming particle striking the topmost surface may not pass
 268 through both lower plates, depending on its trajectory.

269 Assuming a flux $I(\theta)$ of the form in Eq. 5, and evaluating the integral, allows the
 270 simple representation

$$I_D = I_0 A \quad (8)$$

271 where A is an overall geometric factor known as the aperture of the detector, in
 272 units of $\text{m}^2 \text{sr}$. We evaluated the integral according to an exact solution for this detec-
 273 tor geometry given in (Piazelli et al., 1976), and cross-checked with numerical integra-
 274 tion of Eq. 7 using a geometric evaluation of the A_B term, with both calculations giv-
 275 ing exactly $A = 0.3192 \text{ m}^2 \text{sr}$.

276 **4.1.2 Efficiency Corrections**

277 The efficiency of the detection system ϵ , representing the fraction of real events cor-
 278 rectly observed by the detector, must also be evaluated. Firstly the efficiency of the mid-
 279 dle plate was estimated, by comparing the number of events that trigger only the top
 280 and bottom plates $T_{1,3}$ and events that trigger all three plates $T_{1,2,3}$, assuming that $T_{1,3}$
 281 represents true muon events passing through the detector without triggering the mid-
 282 dle plate. Further assuming that each of the three plates has a similar efficiency, the to-
 283 tal efficiency of our detector is given by

$$\epsilon = \left(\frac{T_{1,3}}{T_{1,2,3}} \right)^3 = 94.1\%. \quad (9)$$

284 Dark noise coincidence events and electronics related downtime are estimated to
 285 be negligible.

286 Considering Eqs. 8 and 9, the final expected count rate in s^{-1} would be given sim-
 287 ply by $I_0 A \epsilon$. Rearranging, we can express our own measured value of I_0 by

$$I_M = \frac{C}{A\epsilon T} \quad (10)$$

where C is the total sum of counts over the analysis period and T is the total detection time in seconds (where C was corrected for temperature effects and T for detector uptime as described in Sec. 3.3).

4.2 Muon Flux Correlation with Magnetic Indices

A critical aspect for the monitoring of geomagnetic and space weather activity is the ability for a detector to produce well-calibrated time series data. Firstly, in order to validate the operation of our detector, we define in Section 4.2.1 a statistical test for correlation between our muon data and the Dst index. As a measure of overall geomagnetic activity which is well known to affect the intensity of secondary particle showers at ground level, we expect to see a correlation and thus confirm that our detector is correctly responding to the muon flux over time.

Secondly, it is important to note that during the initial operational phase of our experiment, a particularly strong Forbush decrease occurred on 2024-05-10; a second fairly strong FD occurred on 2024-10-10, which we defined as our second analysis period. As a reference, Figure 8 shows how these events were observed both in the Dst index and in data from the Mexico City neutron monitor, kindly provided by the Cosmic Ray Group of the Geophysical Institute at the National Autonomous University of Mexico (UNAM). The decrease was detected in the neutron monitor approximately two hours after the decrease in Dst, which is consistent with the expected physical delay (Baral et al., 2023; Badruddin et al., 2019). These examples highlight the complementary nature of ground-level particle measurements and geomagnetic observations in identifying space weather disturbances.

Given this opportunity, we also further examined the temporal and morphological relationship between our muon count rate and the Forbush decrease as seen in other magnetic indices, especially the X-component of the magnetic field (which represents the field strength in the Northward direction), as measured nearby within the SAMA region in Vassouras, Brazil.

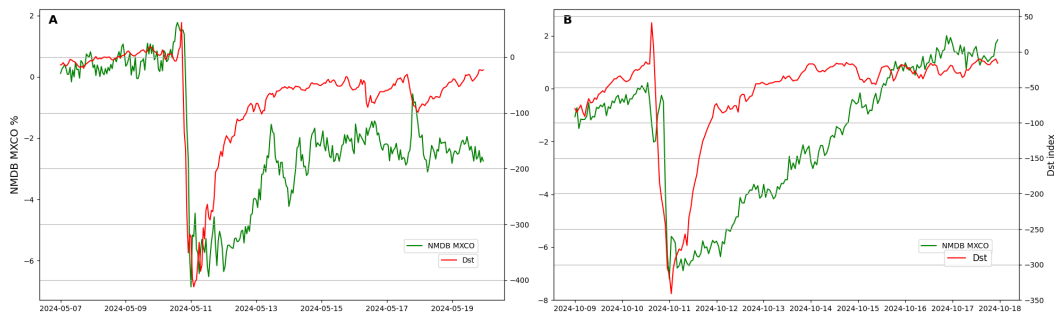


Figure 8: Neutron counts from the Mexico City station of the NMDB plotted alongside the Dst index during the Forbush decrease event on May 10, 2024 (A), and on October 10, 2024 (B).

4.2.1 Dst Comparison – Statistical Methodology

With strong Forbush decreases occurring during our data taking periods, we hope to see an obvious correlation between the Dst index and our muon count rate; nonetheless, before examining the data, we defined a statistical test for the correlation between

319 the two time series. It is a common technique in the field to compare the time-series by
 320 eye, select time ranges, and apply Pearson Correlation Coefficients. However, such meth-
 321 ods lead to over-fitting. Additionally, linear correlations have long been known to give
 322 incorrect results on time series (Yule, 1926) due to autocorrelation or other non-stationary
 323 behaviours (Rodríguez-Poo et al., 2014).

324 In general, there is no perfect method for p -value testing the independence of two
 325 time series, as the choice of alternative hypotheses is not uniquely defined. Of the many
 326 options available, we choose the Truncated Time-Shift (TTS) test (Yuan & Shou, 2024).
 327 The advantages of this test are that it requires only one series to be stationary, and that
 328 it is particularly adept at rejecting false positives. More details can be found in the cited
 329 paper, where a detailed benchmarking of the TTS test is performed against other com-
 330 monly used time-series independence tests on various datasets.

331 The TTS test generates alternative hypotheses by time-shifting one of the input
 332 series. This approach has long been known to under-estimate p values (Bartlett, 1935),
 333 due to the similarity of shifted signals; the TTS test solves this issue by reweighting the
 334 p value, generating instead a statistic called the u -value. For a significance level of $\alpha =$
 335 0.05, then it is shown in (Yuan & Shou, 2024) that if one input series is stationary, then
 336 $P(u \leq \alpha)$ is no more than α . In other words, u can be understood as an “upper limit”
 337 of the traditional p -value, for a given significance α .

338 The TTS test also requires two input parameters. The TTS test is sensitive to time
 339 shifts; if a causal factor affects each series with a different time lag, the test quickly loses
 340 statistical power. This can be accounted for by time-shifting one input series by a lag
 341 l ; this parameter must be known and set before examining the data, to avoid over-fitting.
 342 As described at the beginning of this Section, the expected time delay between the Dst
 343 index and direct particle detection at ground level is approximately two hours (Baral et
 344 al., 2023; Badruddin et al., 2019), therefore for all applications of the TTS test we set
 345 the time shift parameter to $l = +2$ hours. Secondly, the number of alternative hypoth-
 346 eses to generate is not known a priori. As the alternative hypotheses are generated from
 347 clipping and shifting the input data itself, a “truncation radius” r must be set; a higher
 348 r means that less of the time period remains available for final testing, but that more
 349 alternative hypotheses may be generated, and thus the u statistic will have a higher res-
 350 olution. Considering the length of our dataset, and that the Forbush decrease occurred
 351 close to the start of our data, we set a relatively short value of $r = 50$ hours. We adopt
 352 a detection threshold of $u = 0.1$, in analogy with the standard p -value threshold of $p =$
 353 0.05.

354 As this is a recent and lesser known test, to provide an example we first apply it
 355 to the Dst index & NMDB hourly data as was shown in Figure 8A – as these time se-
 356 ries are well-known to be strongly correlated, we expect that the test will be able to re-
 357 ject the null hypothesis of uncorrelated data. The Dst data passes an Augmented Dickey-
 358 Fuller (Dickey & Fuller, 1979) test with $p = 0.001$, which indicates enough stationar-
 359 ity that the TTS test should be applicable. A fairly strong correlation is seen with a TTS
 360 u -value of 0.059.

361 5 Analysis Results

362 5.1 Muon Flux Measurement

363 Our measured average count rate over the analysis period is $C/T = 31.14\text{s}^{-1}$. Thus,
 364 from eq. 10, the measured muon flux at our detector location is:

$$I_M = 103.7 \text{ m}^{-2} \text{ s}^{-1} \text{ sr}^{-1} \quad (11)$$

365 with negligible statistical errors due to the long runtime.

366 This value is reasonable, but towards the higher side when compared with existing
 367 measurements (Borja et al., 2022), which may be related to the location of our de-
 368 tector.

369 5.2 Muon Flux Correlation with Magnetic Indices

370 5.2.1 Dst Index

371 We compare our corrected muon count rate against the Dst index in Figure 9. To
 372 facilitate visual comparison of the two series, the muon count rate is rescaled into a per-
 373 centage change from the initial value, and to match the range of values on the Dst *y*-axis
 374 (in units of nT). The Augmented Dickey-Fuller (ADF) test confirmed stationarity for
 375 both time series, and applying the TTS test as defined, we obtained *u*-values of 0.0196
 376 for the first analysis period and 0.0392 for the second, indicating a statistically signif-
 377 icant correlation in both cases.

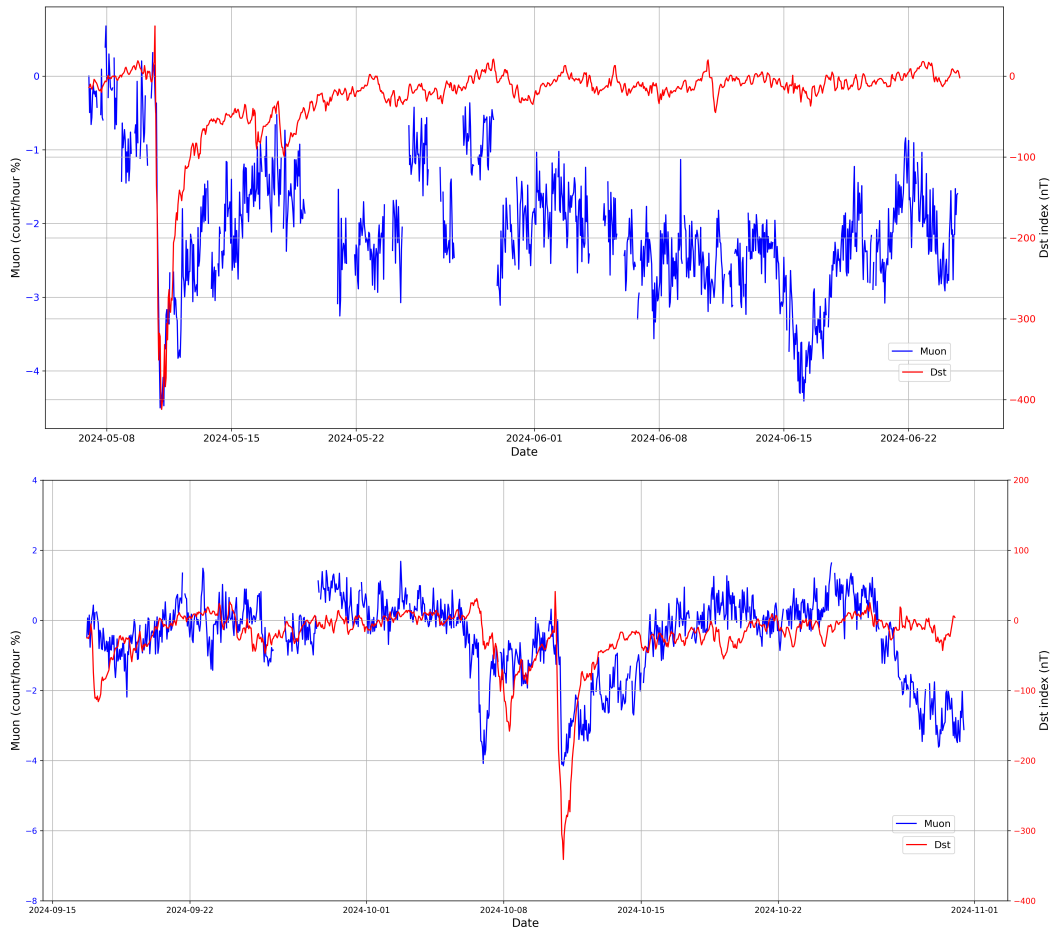


Figure 9: The corrected muon counts compared with the Dst index for each analysis period.

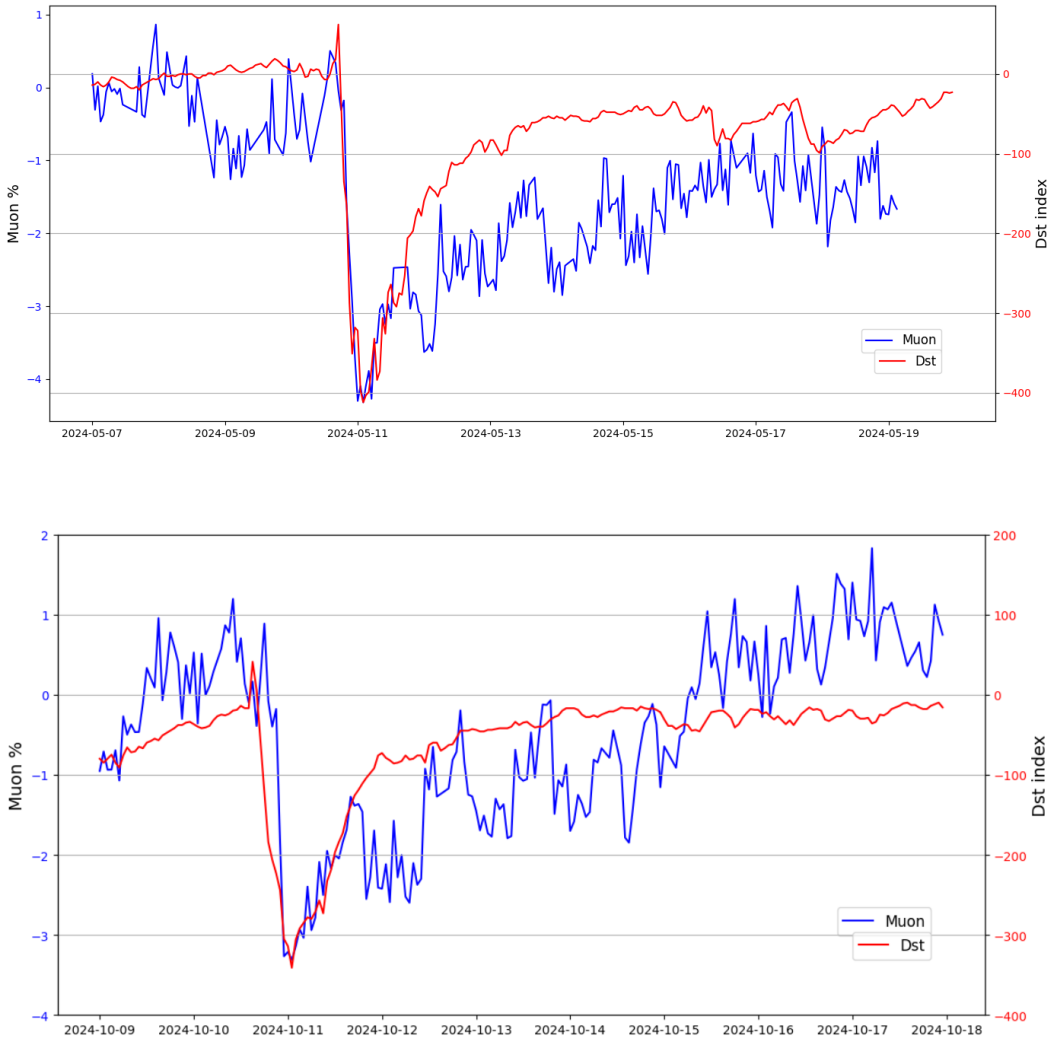


Figure 10: As Fig. 9, but zoomed in on the Forbush decrease events.

In Figure 10, which shows the same muon and Dst comparison but zoomed in on the FD event times, an obvious correlation between the Dst decreases and a drop in muon detection rates in our detector can be seen. Along with the TTS test results on the longer-term dataset, this gives us confidence that our detector is accurately responding to the secondary CR muon flux.

5.2.2 Magnetic Field X-Component

We compare our corrected muon count rate against the X-component of the magnetic field (measured in Vassouras, Brazil) in Figure 11. It can be seen that both signals exhibit a similar temporal profile: a sudden decrease followed by a gradual recovery over several days. The onset of the variation in the X component coincides closely with the initial drop in muon flux (marked as time T_s), suggesting a common solar origin.

This morphological agreement, in both the first and second analysis periods, supports the interpretation that both signatures were caused by the passage of an interplanetary coronal mass ejection (ICME), likely involving a magnetic cloud or shock front. Then, a second magnetic cloud is observed to impact the magnetosphere at time T_1 , cor-

394 responding to the ejecta component of the CME. The cloud fully traverses the magnetosphere by T_2 (as indicated in Figure 4 of (Cane, 2000)).

396 These data agree with the Richardson and Cane ICME catalog (Richardson & Cane,
 397 2025) which identifies the arrival times of interplanetary shocks and the onset of ICMEs.
 398 For the first event, the shock arrival was recorded on May 10, 2024, at 17:05 UT, followed
 399 by the start of the ICME at 20:00 UT on the same day. For the second event, the shock
 400 arrived on October 10, 2024, at 15:14 UT, and the ICME began at 22:00 UT.

401 Such comparisons between ground-based magnetometers and cosmic ray detectors
 402 highlight the complementary nature of these observations in identifying and character-
 403 izing solar-terrestrial disturbances.

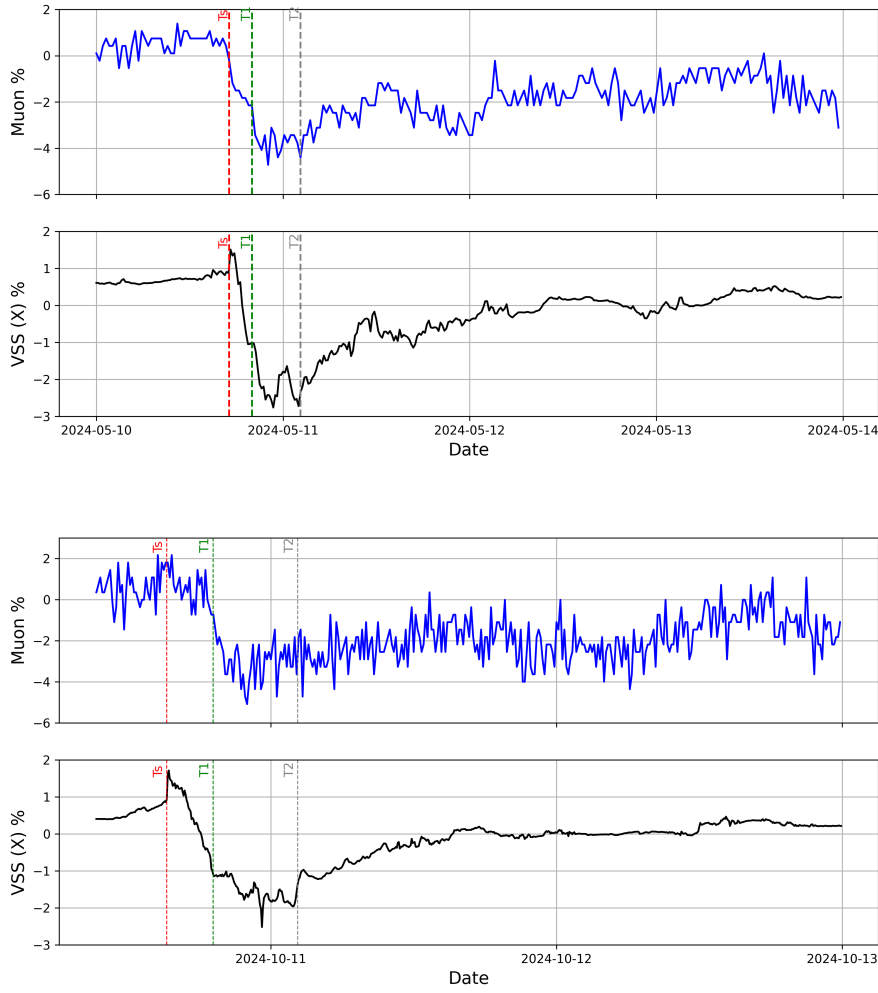


Figure 11: Muon counts during the Forbush events compared with the X component of the magnetic field (measured in Vassouras, Brazil), for both of our analysis periods.

404 6 Discussion and Conclusions

405 We have demonstrated the operation of a new muon detector at ground level within
 406 the SAMA. Despite its compact design and cost-effective implementation, the detector

407 reliably tracks muon flux variations, as shown by its statistically significant ($> 95\%$ confidence)
 408 correlation with the Dst geomagnetic index during two separate analysis periods.
 409 The application of the TTS test here provided a novel and robust statistical method,
 410 minimizing the risk of a spurious result. Our detector was able to clearly identify sev-
 411 eral of the morphological features corresponding to two separate Forbush decrease events.

412 **6.1 Utility of Muon Detectors**

413 Recent developments have shown that muon detectors may play a role in predict-
 414 ing the effects of coronal mass ejections (CMEs). For instance, Ali et al. (2025) demon-
 415 strated that directional measurements of cosmic ray precursors from muon telescopes can
 416 provide advance warnings of CME arrival at Earth, offering valuable lead times for space
 417 weather mitigation, extending up to a full day (Munakata et al., 2020).

418 This is particularly relevant for coordinated forecasting efforts that incorporate mul-
 419 tisensor data, such as solar flare, CME, and radio burst observations. While our detec-
 420 tor currently lacks directional sensitivity, when combined with radio observations from
 421 the CALLISTO spectrometer (Benz et al., 2005) (co-located in Asunción, Paraguay) and
 422 satellite-based solar activity data, the system has potential for early-stage diagnostics
 423 of space weather disturbances, and may enhance the accuracy of SEP and CME arrival
 424 time predictions (González Orué et al., 2023; Kyeremateng et al., 2024).

425 **6.2 Low-Cost Muon Detectors and Global Systems**

426 In agreement with our findings, recent research by (Mubashir et al., 2023) has con-
 427 firmed the effectiveness of low-cost muon detectors for space weather monitoring, show-
 428 ing similar sensitivity to commercial systems during geomagnetic disturbances.

429 The GMDN experiment has also emphasized the significance of coordinated global
 430 muon observations in enhancing the timeliness and reliability of space weather forecasts,
 431 especially in detecting the precursors of interplanetary coronal mass ejections (ICMEs)
 432 (Kihara et al., 2020).

433 Our station in Paraguay addresses an important observational gap in this network,
 434 located in a distinct geophysical region (Saito et al., 2023). This positioning allows for
 435 the collection of data with distinct anisotropic characteristics, contributing to the va-
 436 riety of inputs accessible for global forecasting models. Our work shows that the expan-
 437 sion of such networks with economical detectors is practical, with the potential to sup-
 438 port early warning systems for radiation hazards impacting aviation, satellite operations,
 439 and ground-based infrastructure.

440 **6.3 Future Work**

441 While our results validate the detection system's performance, the high-energy muons
 442 monitored are relatively insensitive to the SAMA's reduced geomagnetic field strength.
 443 To properly characterize the SAMA's effects, future work should target low-energy sec-
 444 ondary photons produced by precipitation of Van Allen belt particles reaching the sur-
 445 face.

446 Current initiatives underway include a high-altitude balloon mission to character-
 447 ize the vertical particle flux profile, enabling ground-to-upper-atmosphere flux compar-
 448 isons, and the development of a low Earth orbit (LEO) satellite payload employing sim-
 449 ilar SiPM-based detectors for direct measurement of high-energy particle precipitation
 450 within the SAMA region.

451 Further studies will expand our instrumentation capabilities, and help improve our
 452 understanding of how geomagnetic and space weather phenomena impacts low-rigidity
 453 environments such as the SAMA.

454 Appendix A Electronic Design Description

455 The following subsections detail individual stages along the signal path, from the
 456 generation of photons, produced by the interaction between charged particles and scin-
 457 tillator plates, to the delivery of modulated pulses to the FPGA board inputs. These stages
 458 include the SiPM polarization circuits and the amplifier circuit board. The amplifier board
 459 operates with regulated supply voltages of $V_{CC} = 5$ V and $V_{EE} = -5$ V. Decoupling
 460 capacitors are included for each integrated circuit in the actual implementation; although
 461 they are shown in most schematics, they are not explicitly discussed in the text.

462 A1 SiPM Polarization Circuit

463 Each S13360-6050VE SiPM embedded in the detector scintillators includes a ded-
 464 icated polarization circuit with a low-pass filter to suppress harmonics and ripple from
 465 the 53.5 V bias supply. The filter consists of a $1\text{ k}\Omega$ resistor and a $0.1\text{ }\mu\text{F}$ capacitor, as
 466 illustrated in Figure A1. When photons interact with the SiPM's photosensitive area,
 467 they generate electrical pulses that are transmitted via SMA-to-MCX cables to the am-
 468 plification board.

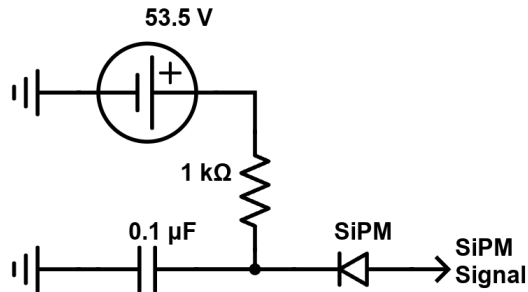


Figure A1: Single SiPM polarization circuit schematic.

469 A2 Transimpedance Amplifier

470 The first stage of the amplification board consists of a transimpedance amplifier
 471 implemented with an OPA847, configured as a summing amplifier with a gain of 100,
 472 as illustrated in Figure A2. Capacitors are placed at the non-inverting input and within
 473 the feedback loop, while RC networks are connected from the inverting input and the
 474 output to ground to improve signal stability, in accordance with the OPA847 datasheet
 475 recommendations. The RC network connected to the non-inverting input also serves to
 476 set a zero-level reference when no SiPM signals are present.

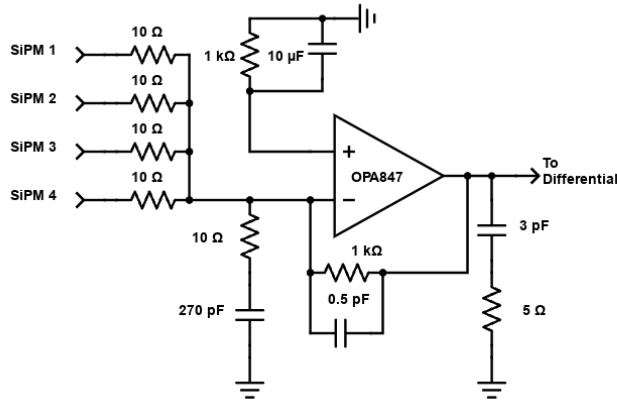


Figure A2: Transimpedance amplifier circuit for a single channel.

A3 Differential Amplifier

A THS4131 differential amplifier is used to decouple the flowing signal from an analog output, which was used in early testing stages for signal characterization. The transimpedance output and ground serve as the differential inputs. To preserve the shape of the output pulses, resistor values of $374\ \Omega$ at the inputs and $750\ \Omega$ in the feedback paths were selected, following the recommendations in the THS4131 datasheet, as illustrated in Figure A3. Capacitors were added at the inputs and within the feedback loops to improve signal stability. A $49.9\ \Omega$ resistor is connected to the analog output to serve as probe impedance for oscilloscopes.

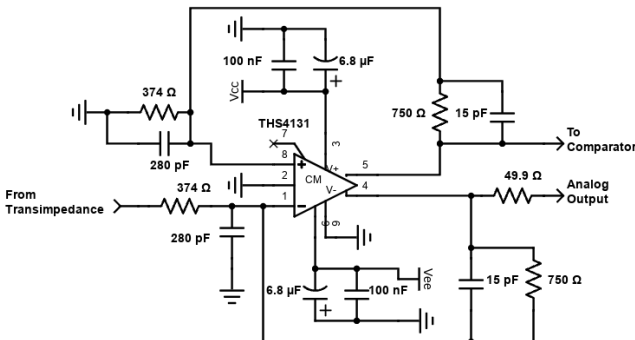


Figure A3: Differential amplifier circuit for a single channel.

A4 Reference Voltage Circuit

A reference voltage, individually calibrated for each channel, is generated using a user-set AD5270-100 digital potentiometer of $100\ k\Omega$, which is controlled by the FPGA. The desired resistance value is defined in a configuration file and set via digital control signals. This potentiometer is part of a resistive divider with a $750\ k\Omega$ resistor, producing a reference voltage that is then buffered to ensure signal path decoupling and to maintain a linear relationship between the configured resistance value and the output threshold voltage. The buffered signal is passed through an inverter to obtain a negative reference voltage, required for the hysteresis comparator stage, as illustrated in Figure A4.

495 An LM358 dual operational amplifier is used to implement the buffering and inversion
 496 stages.

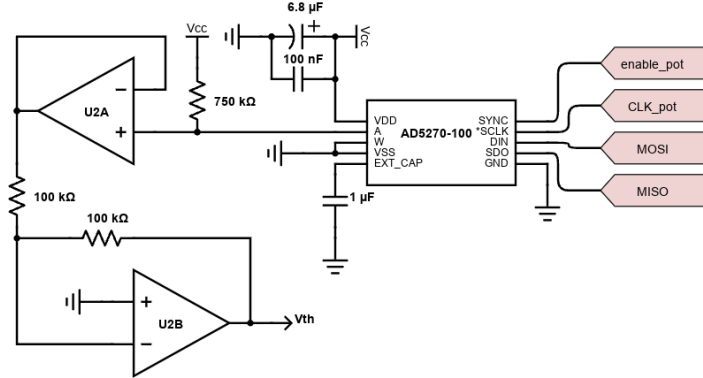


Figure A4: Reference voltage circuit for a single channel.

497 A5 Hysteresis Comparator

498 The reference voltage and the output of the differential amplifier serve as inputs
 499 to a hysteresis comparator circuit based on the TL3116. This stage is used to reject pulses
 500 identified as noise during the calibration process. The comparator implements a calcu-
 501 lated hysteresis of 2.1 mV , using 470Ω resistors at the inputs and $1 \text{ M}\Omega$ resistors in the
 502 feedback paths. A 100 nF decoupling capacitor is also placed at the reference voltage
 503 input, as illustrated in Figure A5. The comparator produces output pulses of 2.5 V with
 504 a duration of approximately 100 ns , which are then passed to the time-stretching cir-
 505 cuit.

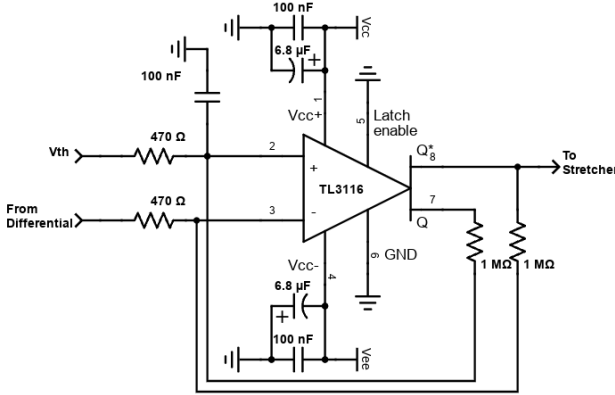


Figure A5: Hysteresis comparator circuit for a single channel.

506 A6 Time Stretching Circuit

507 The signal is modulated in time to produce a discrete pulse compatible with the
 508 3.3V CMOS logic levels of the Basys 3 FPGA. This modulation is implemented using
 509 an array of NAND and NOT gates, as illustrated in Figure A6. A 47Ω resistor and a
 510 $0.015 \mu\text{F}$ capacitor set the output pulse width, yielding a period of approximately 493.5 ns ,
 511 according to $T_{\text{out}} = 0.7 \cdot R \cdot C$. The output is routed to dedicated FPGA input pins

512 through $80\ \Omega$ series resistors, which provide signal termination and help minimize reflections.
 513

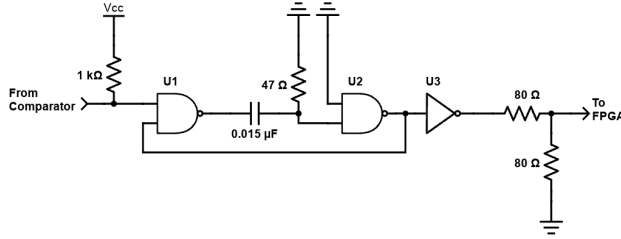


Figure A6: Time stretching circuit for a single channel.

514 A7 FPGA Board Connection

515 Each signal path from the individual channels terminates at a dedicated input pin
 516 on the Basys3 FPGA development board, while control signals for the digital potentiome-
 517 ters connect to separate I/O ports. A resistive voltage divider, consisting of $2.2\ k\Omega$ and
 518 $3.3\ k\Omega$ resistors, is implemented for the MISO signal to ensure compatibility with the
 519 $3.3\ V$ CMOS logic level, as illustrated in Figure A7. Additionally, a mini USB port with
 520 UART logic enables communication with the computer.

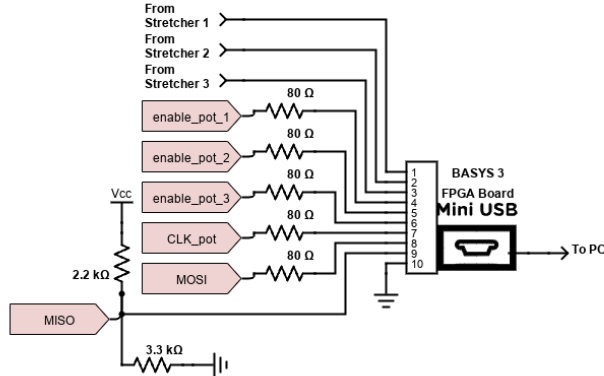


Figure A7: Basys3 FPGA connections in the amplification circuit board.

521 Appendix B Muon Flux Correlation with Neutron Flux

522 In addition to the time series comparisons between the Dst index and the local mag-
 523 netic field, Figure B1 compares our muon count rate with the neutron count rate recorded
 524 by the NMDB detector in Mexico, with variation rates in percentages. This detector is
 525 chosen based on its similar cutoff rigidity, but distinct hemispheric location, mirroring
 526 the latitude of the SAMA.

527 We include this information in the appendix as it is in some sense a redundant test,
 528 as we compared both our muon rate and the NMDB count rate to the Dst index indi-
 529 vidually, and since we would expect that both instruments would respond to disturbances
 530 in a similar way. However, this could be seen as an additional check confirming the func-
 531 tioning of our muon detector.

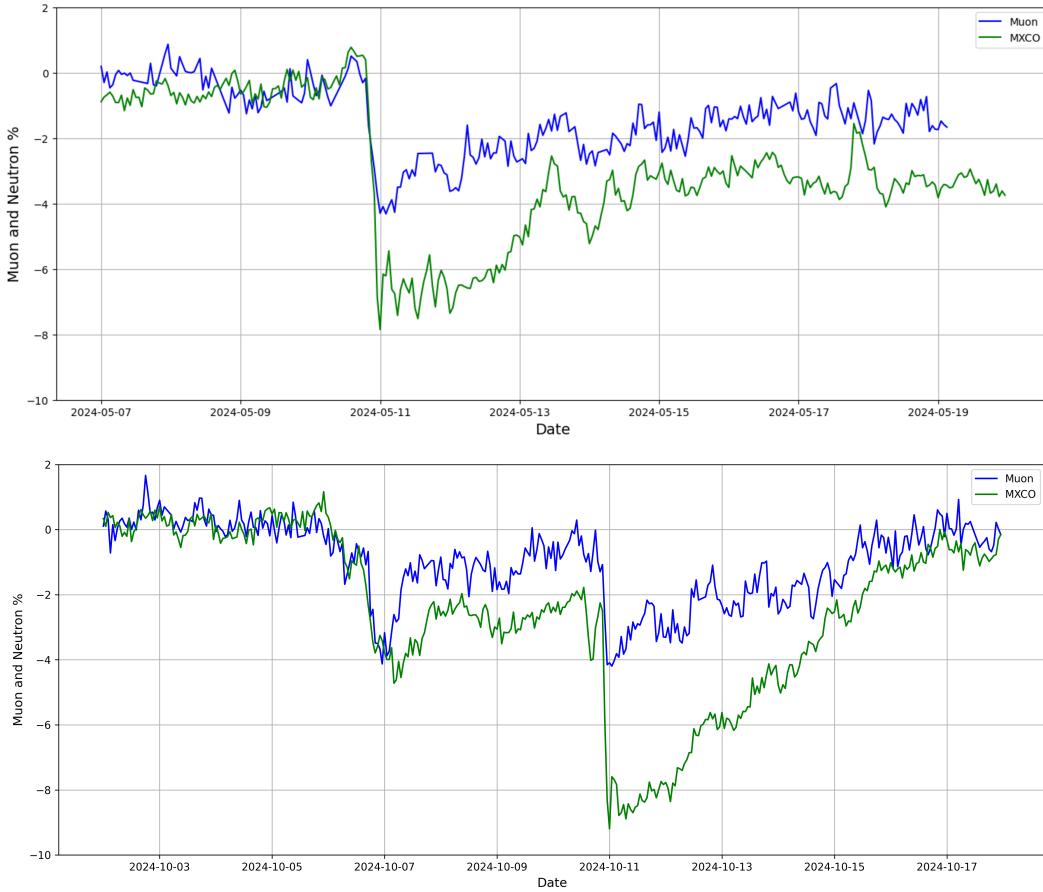


Figure B1: Neutron counts from the Mexico station of the NMBD, plotted together with the muon rate from our detector, for both analysis periods. The *y*-axes show percentage variations from the initial value of each series, per hour.

532 Additionally, the neutron monitor also sees a depression around October 6, which
 533 was also seen in our detector, but whose origin remained unclear due to not being as-
 534 sociated with a strong magnetic storm (and the technical issue of partial failure of our
 535 temperature control units). These events also highlight the need for global detection sys-
 536 tems with high coverage, which will allow us to investigate such events in more detail.

537 Acknowledgments

538 The authors acknowledge the financial support given by the Engineering Faculty
 539 (FIUNA). Authors JM and DHS acknowledge the FEEI-PROCIENCIA-CONACYT-PRONII.

540 Open Research: Availability Statement

541 The datasets underpinning the study, are openly accessible in the Zenodo repos-
 542 itory (Molina et al., 2025). These datasets encompass time series of muon flux measure-
 543 ments, Disturbance Storm Time (Dst) index values, and neutron monitor data for both
 544 observation periods: May 2024 and October 2024.

545 The analysis code employed in this research, which includes the Jupyter Notebook
 546 detailing data processing and the implementation of the Truncated Time-Shift (TTS)

547 test for time-series correlation analysis, is available in the GitHub repository: <https://github.com/diegostaPy/ForbushDecrease-SAMA->. This repository ensures transparency
 548 and reproducibility of the study's findings.
 549

550 All datasets and software are licensed under the Creative Commons Attribution
 551 4.0 International License (CC BY 4.0), permitting unrestricted use, distribution, and re-
 552 production in any medium, provided the original work is properly cited.

553 References

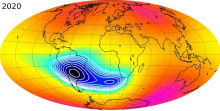
- 554 Ali, M. A., Abdelkawy, A. G. A., Shaltout, A. M. K., & Beheary, M. M. (2025).
 555 Forecasting solar energetic particles using multi-source data from solar flares,
 556 cmes, and radio bursts with machine learning approaches. *Scientific Reports*,
 557 15(1), 9546. Retrieved from <https://doi.org/10.1038/s41598-025-92207-1>
 558 doi: 10.1038/s41598-025-92207-1
- 559 AMD. (2024a). *Amd microblaze™ micro controller system (mcs)*. Website.
 560 Retrieved from <https://www.amd.com/en/products/software/adaptive-socs-and-fpgas/mb-mcs.html> (Accessed 2024-11-27)
- 562 AMD. (2024b). *Amd vitis™ unified software platform*. Website. Retrieved from
 563 <https://www.amd.com/en/products/software/adaptive-socs-and-fpgas/vitis.html> (Accessed 2024-11-27)
- 565 AMD. (2024c). *Amd vivado™ design suite*. Website. Retrieved from <https://www.amd.com/en/products/software/adaptive-socs-and-fpgas/vivado.html>
 566 (Accessed 2024-11-27)
- 568 Augusto, C. R. A., Kopenkin, V., Navia, C. E., Tsui, K. H., Shigueoka, H.,
 569 Fauth, A. C., ... Velarde, A. (2012, nov.). Variations of the muon flux
 570 at sea level associated with interplanetary icmes and corotating inter-
 571 action regions. *Astrophysical Journal*, 759(2), 143. Retrieved from
 572 <https://ui.adsabs.harvard.edu/abs/2012ApJ...759..143A> doi:
 573 10.1088/0004-637X/759/2/143
- 574 Augusto, C. R. A., Navia, C. E., Tsui, K. H., Shigueoka, H., Miranda, P., Ticona,
 575 R., ... Saavedra, O. (2010). Simultaneous observation at sea level and at 5200
 576 m.a.s.l. of high energy particles in the south atlantic anomaly. *Astroparticle
 577 Physics*, 34. doi: 10.1016/j.astropartphys.2010.04.005
- 578 Badruddin, B., Aslam, O. P. M., Derouich, M., Asiri, H., & Kudela, K. (2019).
 579 Forbush decreases and geomagnetic storms during a highly disturbed solar
 580 and interplanetary period, 4–10 september 2017. *Space Weather*, 17(3), 487–
 581 496. Retrieved from <https://agupubs.onlinelibrary.wiley.com/doi/abs/10.1029/2018SW001941> doi: 10.1029/2018SW001941
- 583 Baral, R., Adhikari, B., Calabia, A., Shah, M., Mishra, R. K., Silwal, A., ...
 584 Rodríguez Frías, M. D. (2023). Spectral features of forbush decreases dur-
 585 ing geomagnetic storms. *Journal of Atmospheric and Solar-Terrestrial Physics*,
 586 242, 105981. Retrieved from <https://www.sciencedirect.com/science/article/pii/S1364682622001547> doi: 10.1016/j.jastp.2022.105981
- 588 Bartlett, M. S. (1935). Some aspects of the time-correlation problem in regard to
 589 tests of significance. *Journal of the Royal Statistical Society*, 98(3), 536–543.
 590 Retrieved 2025-05-20, from <http://www.jstor.org/stable/2342284>
- 591 Benz, A., Monstein, C., & Meyer, H. (2005, oct). Callisto - a new concept for so-
 592 lar radio spectrometers. *Solar Physics*, 226, 143–151. doi: 10.1007/s11207-005
 593 -5688-9
- 594 Bertoli, M., Secchia, G., Molina Insfrán, J. A., Cristaldo Morales, E. J., Ben-
 595 itez Montiel, C. G., & Cuevas Mongelós, A. (2023). Optimization of a
 596 muon detection system with silicon photomultiplier sensors (sipm). In
 597 *2023 ieee chilean conference on electrical, electronics engineering, in-
 598 formation and communication technologies (chilecon)* (pp. 1–6). doi:

- 599 10.1109/CHILECON60335.2023.10418659
- 600 Borja, C., Ávila, C., Roque, G., & Sánchez, M. (2022). Atmospheric muon flux
601 measurement near earth's equatorial line. *Instruments*, 6(4), 78. Retrieved from <https://www.mdpi.com/2410-390X/6/4/78> doi: 10.3390/instruments6040078
- 602
- 603 Borovsky, J. E., & Shprits, Y. Y. (2017). Is the dst index sufficient to define all
604 geospace storms? *Journal of Geophysical Research: Space Physics*, 122(11),
605 11543–11547. Retrieved from <https://agupubs.onlinelibrary.wiley.com/doi/abs/10.1002/2017JA024679> doi: 10.1002/2017JA024679
- 606
- 607 Cane, H. (2000). Coronal mass ejections and forbush decreases. *Space Science Reviews*,
608 93. Retrieved from <https://www.osti.gov/biblio/4554034>
- 609 Dickey, D., & Fuller, W. (1979, 06). Distribution of the estimators for autoregressive
610 time series with a unit root. *Journal of the American Statistical Association*, 74. doi: 10.2307/2286348
- 611
- 612 Digilent. (2024). *Basys 3 reference*. Website. Retrieved from <https://digilent.com/reference/basys3/refmanual> (Accessed September 26, 2024)
- 613
- 614 Dinu, N. (2016). 8 - silicon photomultipliers (sipm). In B. Nabet (Ed.), *Photodetectors* (p. 255-294). Woodhead Publishing. Retrieved from <https://www.sciencedirect.com/science/article/pii/B9781782424451000087> doi: 10.1016/B978-1-78242-445-1.00008-7
- 615
- 616 Dorman, L. I. (1974). Cosmic rays: Variations and space explorations.. Retrieved
617 from <https://api.semanticscholar.org/CorpusID:120880781>
- 618
- 619 Eljen Technology. (2024). *General purpose ej-200, ej-204, ej-208, ej-212*. Website.
620 Retrieved from <https://eljentechnology.com/products/plastic-scintillators/ej-200-ej-204-ej-208-ej-212> (Accessed September 26, 2024)
- 621
- 622 Fauth, A. (2016). Forbush decreases detected by the muonca muon telescopes on 13
623 september and 22 december 2014. *PoS, ICRC2015*, 073. doi: 10.22323/1.236
624 .0073
- 625
- 626 Finlay, C. C., Kloss, C., Olsen, N., Hammer, M. D., Tøffner-Clausen, L., Grayver,
627 A., & Kuvshinov, A. (2020). The chaos-7 geomagnetic field model and ob-
628 served changes in the south atlantic anomaly. *Earth, Planets and Space*, 72(1),
629 156. Retrieved from <https://doi.org/10.1186/s40623-020-01252-9> doi:
630 10.1186/s40623-020-01252-9
- 631
- 632 Frigo, E., Savian, J., Rockenbach, M., Dal Lago, A., & Schuch, N. (2007). Analysis
633 of geomagnetic storm variations and count-rate of cosmic ray muons recorded
634 at the brazilian southern space observatory. *Revista Brasileira de Geofísica*,
635 25. doi: 10.1590/S0102-261X2007000600018
- 636
- 637 Friis-Christensen, E., Lühr, H., & Hulot, G. (2006). Swarm: A constellation
638 to study the earth's magnetic field. *Earth, Planets and Space*, 58(4),
639 351–358. Retrieved from <https://doi.org/10.1186/BF03351933> doi:
640 10.1186/BF03351933
- 641
- 642 González Orué, I., Stalder, D., Salgueiro, L., & Molina, J. (2023). Automatic solar
643 radio burst detection using deep learning. In *2023 ieee chilean conference on
644 electrical, electronics engineering, information and communication technologies
(chilecon)* (pp. 1–6). doi: 10.1109/CHILECON60335.2023.10418691
- 645
- 646 Greisen, K. (1942, mar). The intensities of the hard and soft components of cos-
647 mic rays as functions of altitude and zenith angle. *Phys. Rev.*, 61(5-6), 212–
648 221. Retrieved from <https://link.aps.org/doi/10.1103/PhysRev.61.212> doi: 10.1103/PhysRev.61.212
- 649
- 650 Kihara, K., Munakata, K., Kato, C., Yasue, S., Akahane, S., Koyama, M., ...
651 Kuwabara, T. (2020). Three-dimensional anisotropy of galactic cosmic rays
652 in successive solar rotations. *The Astrophysical Journal*, 900(2), 75. doi:
653 10.3847/1538-4357/abad92
- 654 Kilifarska, N. A., Bakhmutov, V. G., & Melnyk, G. V. (2020). Chapter 5. galactic

- cosmic rays and solar particles in earth's atmosphere: Section 5.1.1.2. short-term variations. In N. A. Kilifarska, V. G. Bakhmutov, & G. V. Melnyk (Eds.), *The hidden link between earth's magnetic field and climate* (pp. 101–131). Elsevier. Retrieved from <https://www.sciencedirect.com/science/article/pii/B978012819346400005X> doi: 10.1016/B978-0-12-819346-4.00005-X
- Klein, K.-L., Steigies, C. T., Wimmer-Schweingruber, R. F., Kudela, K., Strharsky, I., Langer, R., ... García-Población, O. (2010, January). [Www.nmdb.eu](http://www.nmdb.eu): The real-time neutron monitor database. In *38th cospar scientific assembly* (Vol. 38, p. 3). Retrieved from <https://ui.adsabs.harvard.edu/abs/2010cosp...38.1685K>
- Kovyljaeva, A. A., Dmitrieva, A. N., Tolkacheva, N. V., & Yakovleva, E. I. (2013, February). Calculations of temperature and barometric effects for cosmic ray flux on the earth surface using the corsika code. *Journal of Physics: Conference Series*, 409(1), 012128. Retrieved from <https://dx.doi.org/10.1088/1742-6596/409/1/012128> doi: 10.1088/1742-6596/409/1/012128
- Kyeremateng, K., Hamada, A., Elsaïd, A., & Mahrouz, A. (2024, Jun 5). Deep learning-based prediction of cme-driven shock standoff distances in metric type ii radio emissions. *Astrophysics and Space Science*, 369(6), 57. Retrieved from <https://doi.org/10.1007/s10509-024-04319-1> doi: 10.1007/s10509-024-04319-1
- Mendonça, R. R. S., Braga, C. R., Echer, E., Dal Lago, A., Munakata, K., Kuwabara, T., ... Sabbah, I. (2016, oct). The temperature effect in secondary cosmic rays (muons) observed at the ground: Analysis of the global muon detector network data. *The Astrophysical Journal*, 830(2), 88. Retrieved from <https://dx.doi.org/10.3847/0004-637X/830/2/88> doi: 10.3847/0004-637X/830/2/88
- Molina, J., Richard, E., Giovanni, S., Stalder, D., Bertoli, M., Trepowski, C., ... Cuevas, A. (2025). *Measurements of forbush decrease events at the center of the south atlantic magnetic anomaly with muon detectors*. Zenodo. Retrieved from <https://doi.org/10.5281/zenodo.15032283> doi: 10.5281/zenodo.15032283
- Mppc (multi-pixel photon counter) s13360-2050ve/-3050ve/-6050ve [Computer software manual]. (2024). Retrieved from https://www.hamamatsu.com/content/dam/hamamatsu-photonics/sites/documents/99_SALES_LIBRARY/ssd/s13360-2050ve_etc_kapd1053e.pdf
- Mubashir, A., Ashok, A., Bourgeois, A. G., Chien, Y. T., Connors, M., Potdevin, E., ... Tiwari, C. (2023). Muon flux variations measured by low-cost portable cosmic ray detectors and their correlation with space weather activity. *Journal of Geophysical Research: Space Physics*, 128(12), e2023JA031943. doi: 10.1029/2023JA031943
- Munakata, K., Kato, C., Yasue, S., Kihara, K., Akahane, S., Koyama, M., ... Schuch, N. J. (2020). Real-time cosmic ray monitoring system for space weather. *Space Weather*, 18(3), e2020SW002497. doi: 10.1029/2020SW002497
- National Centers for Environmental Prediction (NCEP). (n.d.). *National centers for environmental prediction*. Website. Retrieved from <https://www.noaa.gov/jetstream/ncep> (Accessed 2024-12-10)
- National Oceanic and Atmospheric Administration (NOAA). (n.d.). *Global data assimilation system (gdas)*. Website. Retrieved from <https://www.ncei.noaa.gov/products/weather-climate-models/global-data-assimilation> (Accessed 2024-12-10)
- Nose, M., Iyemori, T., Sugiura, M., & Kamei, T. (2015). *Geomagnetic dst index*. (World Data Center for Geomagnetism, Kyoto) doi: 10.17593/14515-74000

- 708 Papailiou, M.-C., Abunina, M., Mavromichalaki, H., Shlyk, N., Belov, S., Abunin,
 709 A., ... Triantou, A. (2024). Precursory signs of large forbush decreases in
 710 relation to cosmic rays equatorial anisotropy variation. *Atmosphere*, 15(7),
 711 742. Retrieved from <https://www.mdpi.com/2073-4433/15/7/742> doi:
 712 10.3390/atmos15070742
- 713 Pavón-Carrasco, F. J., & De Santis, A. (2016). The south atlantic anomaly: The key
 714 for a possible geomagnetic reversal. *Frontiers in Earth Science*, 4. Retrieved
 715 from <https://www.frontiersin.org/journals/earth-science/articles/10.3389/feart.2016.00040> doi: 10.3389/feart.2016.00040
- 716 Piazolli, B., Mannocchi, G., Melone, S., Picchi, P., & Vicentini, R. (1976, 1). Aperture
 717 and counting rate of rectangular telescopes for single and multiple parallel
 718 particles. *Nuclear Instruments and Methods*, 135.
- 719 Pinto, O. J., Kirchhoff, V. W. J. H., & Gonzalez, W. D. (1990, may). Mesospheric
 720 ozone depletion due to energetic electron precipitation at the south
 721 atlantic magnetic anomaly. *Annales Geophysicae*, 8, 365–367. Retrieved from
 722 <https://ui.adsabs.harvard.edu/abs/1990AnGeo...8..365P> (Provided by
 723 the SAO/NASA Astrophysics Data System)
- 724 Richardson, I., & Cane, H. (2025). Website. Retrieved from <https://izw1.caltech.edu/ACE/ASC/DATA/level3/icmetable2.htm> (Accessed 2025-05-01) doi: 10
 725 .7910/DVN/C2MHTH
- 726 Riádigos, I., García-Castro, D., González-Díaz, D., & Pérez-Muñuzuri, V. (2020).
 727 Atmospheric temperature effect in secondary cosmic rays observed with a 2
 728 square meter ground-based trpc detector. *Earth and Space Science*, 7(9),
 729 e2020EA001131. Retrieved from <https://agupubs.onlinelibrary.wiley.com/doi/abs/10.1029/2020EA001131> doi: 10.1029/2020EA001131
- 730 Rockenbach, M., Dal Lago, A., Schuch, N. J., Munakata, K., Kato, C., Kuwabara,
 731 T., ... Sabbah, I. (2014). South atlantic magnetic anomaly impacts on the
 732 inner radiation belt particle fluxes. *Journal of Geophysical Research: Space
 733 Physics*, 119(12), 9841–9859. doi: 10.1002/2014JA020580
- 734 Rodríguez-Poo, J., Moral, I., Aparicio, T., Villanúa, I., Cizek, P., Xia, Y., ...
 735 Cížková, L. (2014). *Computer-aided introduction to econometrics*. Springer
 736 Science & Business Media.
- 737 Saito, T., Miyoshi, Y., Seki, K., Matsumoto, Y., Asamura, K., Takashima, T., ...
 738 Higashio, N. (2023). Radiation environment monitoring in the south atlantic
 739 anomaly. *Journal of Space Weather and Space Climate*, 13, 27. doi:
 740 10.1051/swsc/2023024
- 741 Schuch, N. J. (2013). The global muon detector network - gmdn the brazilian contribu-
 742 tion for space weather forecasting. In *33rd international cosmic ray confer-
 743 ence* (p. 0946).
- 744 Yuan, A., & Shou, W. (2024). A rigorous and versatile statistical test for cor-
 745 relations between stationary time series. *PLOS Biology*, 22(8), 1–26. Re-
 746 trieval from <https://doi.org/10.1371/journal.pbio.3002758> doi:
 747 10.1371/journal.pbio.3002758
- 748 Yule, G. U. (1926). Why do we sometimes get nonsense-correlations between time-
 749 series?—a study in sampling and the nature of time-series. *Journal of the Royal
 750 Statistical Society*, 89(1), 1–63. Retrieved 2024-07-10, from <http://www.jstor.org/stable/2341482>

Figure 1.



32000

32000

32000

32000

32000

nT

Figure 2.



Arriba

Figure 3.

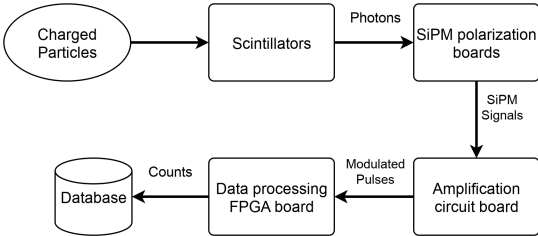


Figure 4.

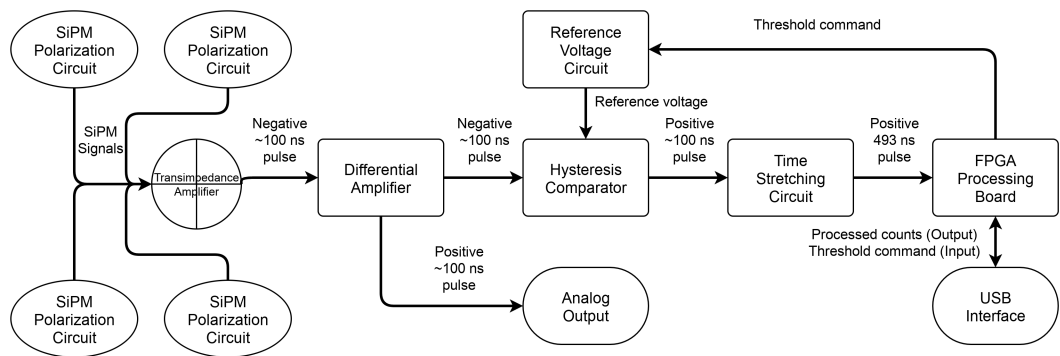


Figure 5.

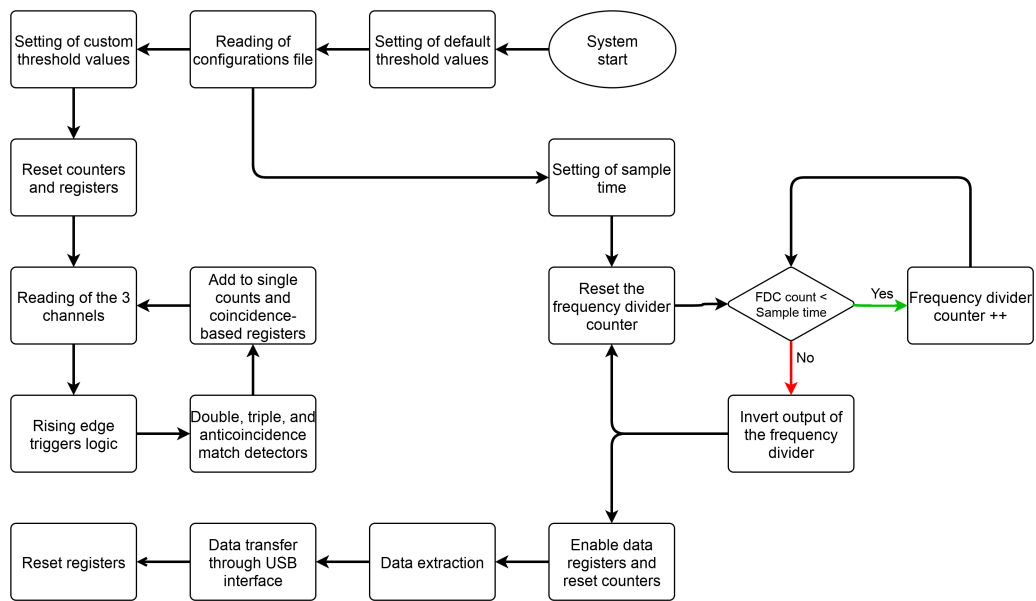


Figure 6.

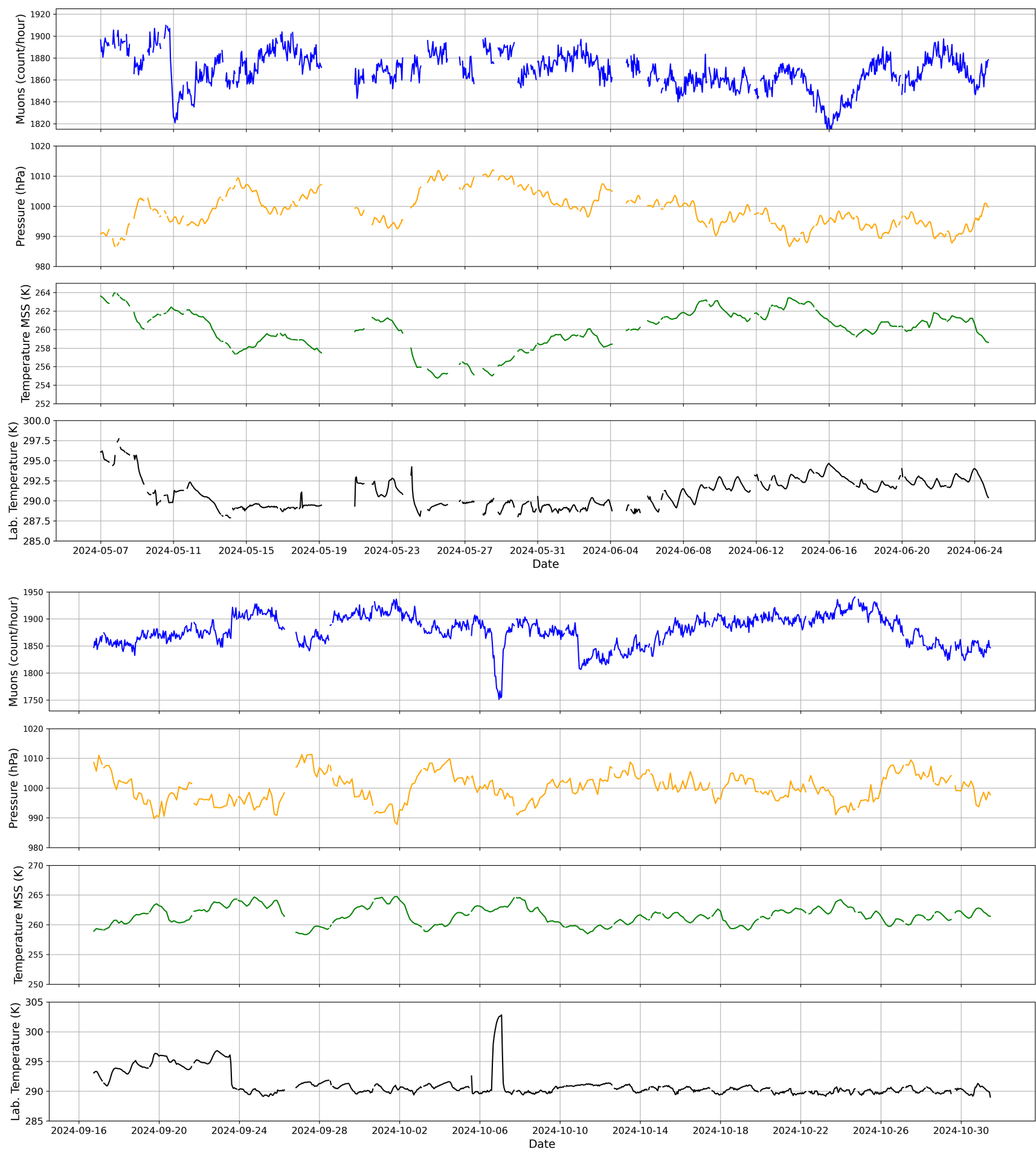


Figure 7.

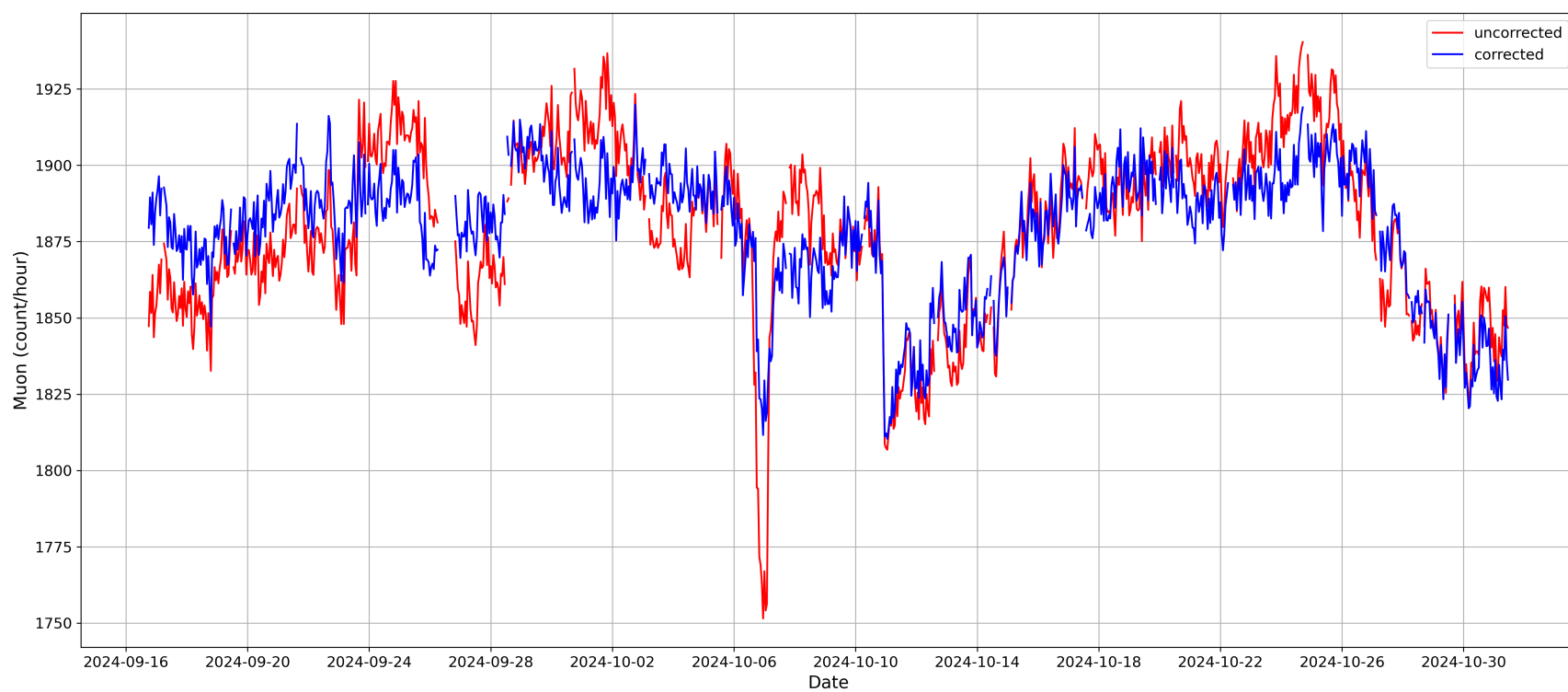
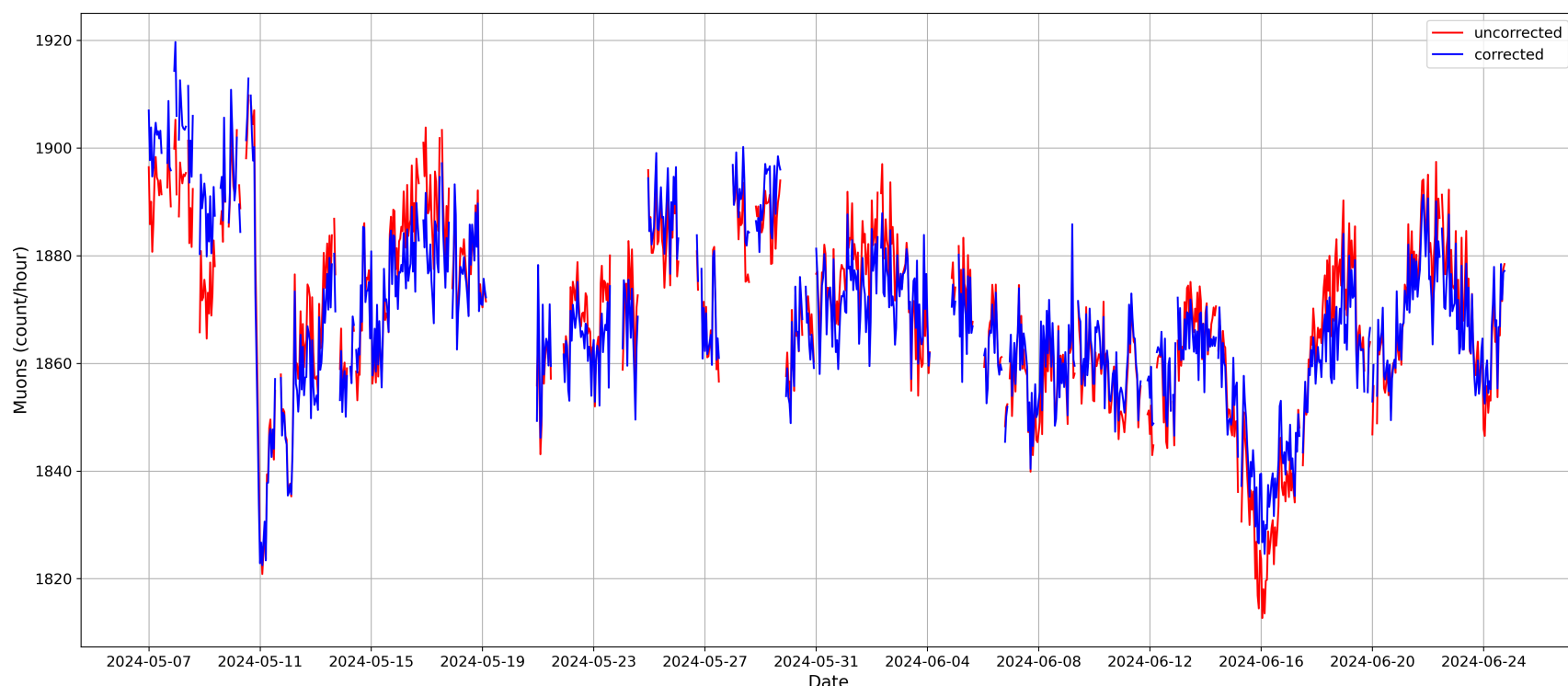


Figure 8.

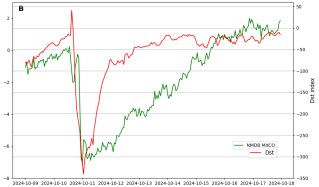


Figure 9.

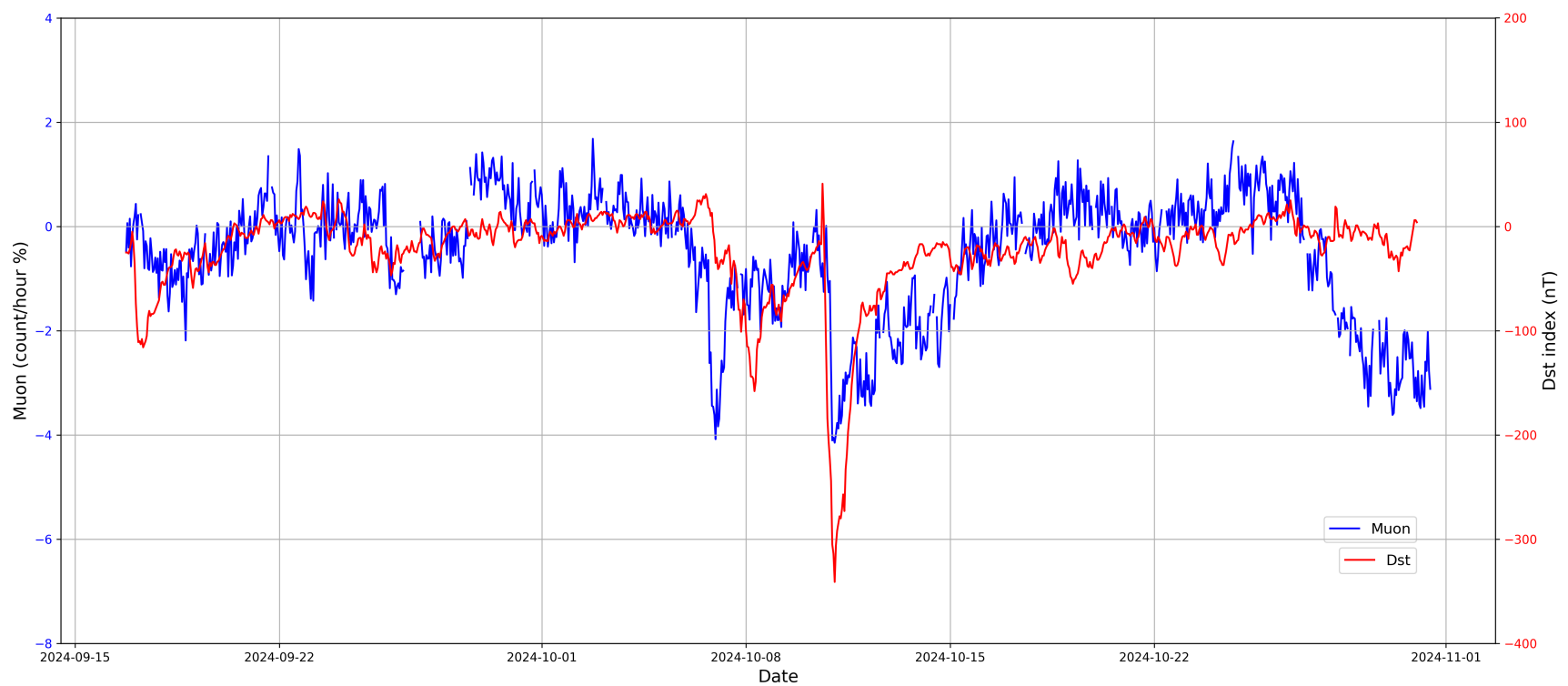
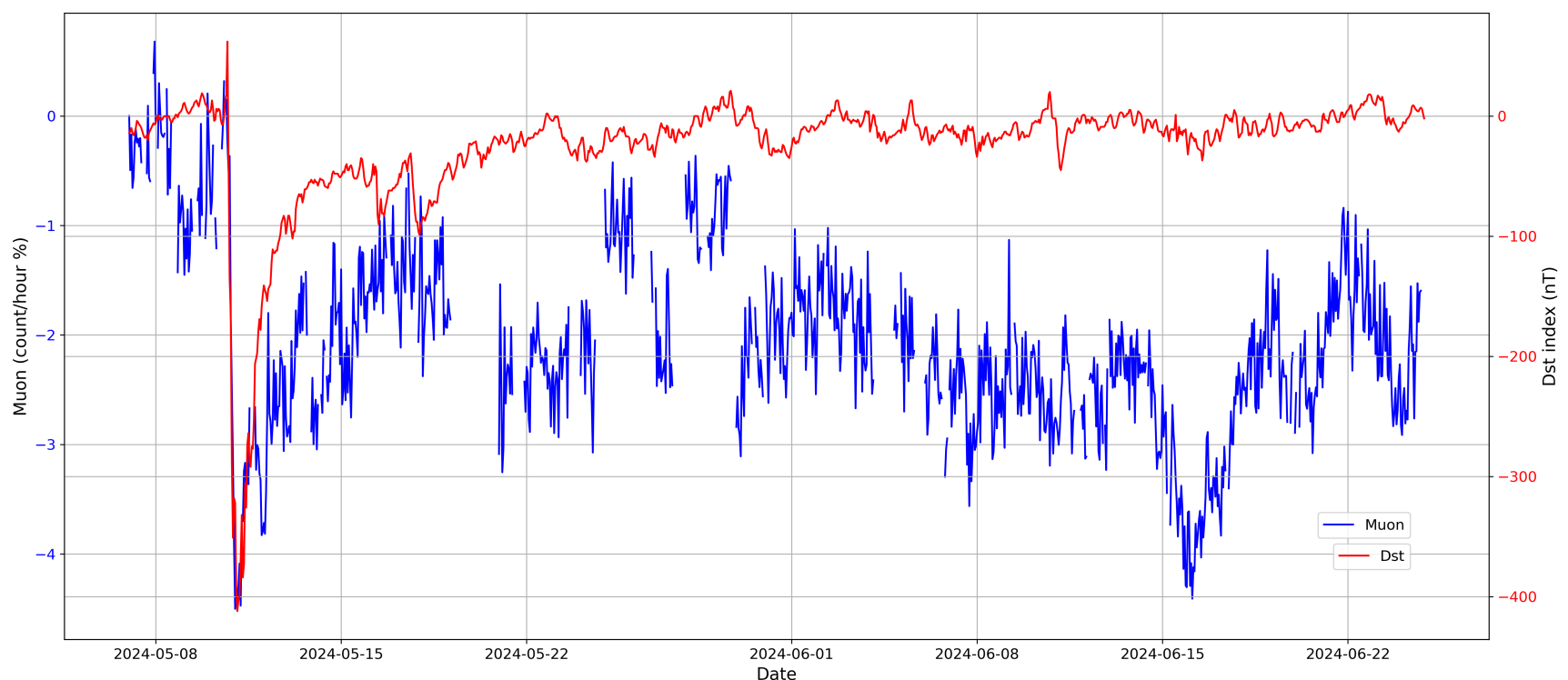


Figure 10.

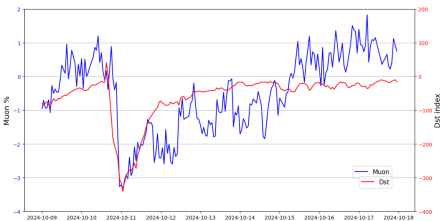


Figure 11.

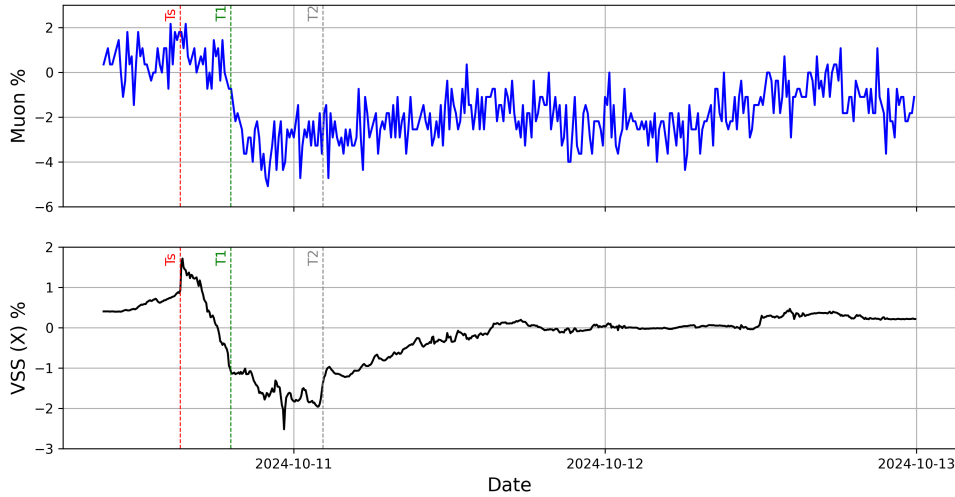
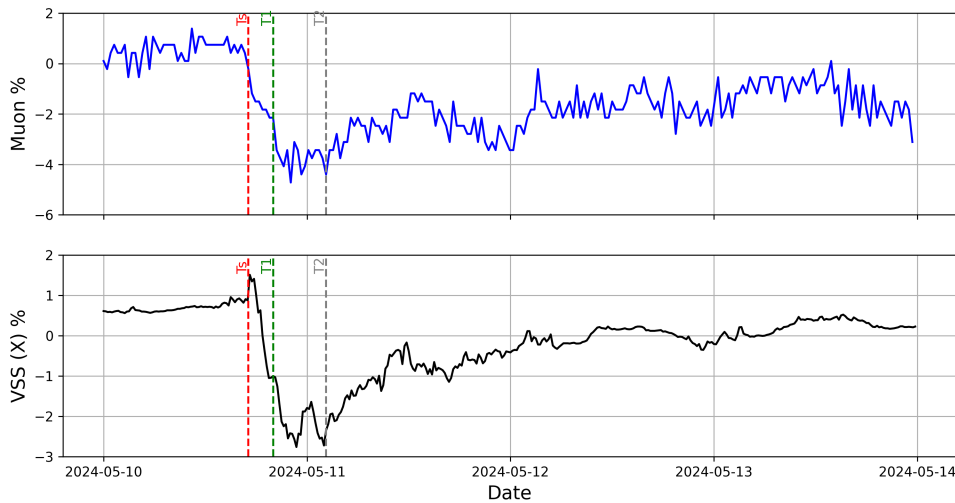


Figure A1.

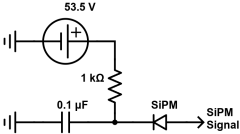


Figure A2.

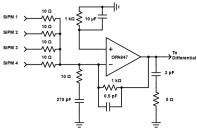


Figure A3.

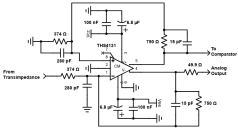


Figure A4.

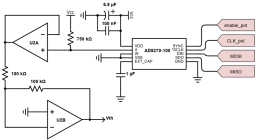


Figure A5.

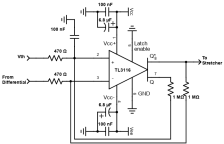


Figure A6.

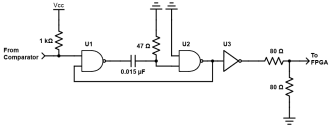


Figure A7.

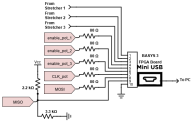


Figure B1.

